Sound Wave Scattering by Cylindrical Shells with Internal Structures

by

Sewon Park

B. S. Seoul National University (1988)
S. M. Massachusetts Institute of Technology (1992)

Submitted to the Department of
Ocean Engineering in the Partial Fulfillment of
the Requirements for the
Degree of

Ocean Engineer
at the

Massachusetts Institute of Technology

February 1995

Signature of Author . . . . . .
Department of Ocean Engineering
January, 1995

Certified by . . . . . .
Professor Ira Dyer
Thesis Supervisor

Accepted by . . . . . .
Professor A. Douglas Carmichael
Chairman, Department Graduate Committee

Sound Wave Scattering by Cylindrical Shells with Internal Structures

by Sewon Park

Submitted to the Department of Ocean Engineering in partial fulfillment of the requirements for the Ocean Engineer degree

Abstract

In this thesis I study the mid-frequency scattering properties at beam incidence from different kinds of cylindrical shells; empty shell, shell with stiffening rings, shell with internal structures only and layered shell, the latter having the same internal structures. The measurements and analyses were conducted over a mid-frequency range of $2 < ka < 12$, where k is the acoustic wave number in water and a is the radius of the shell. Both time and frequency domain representations of the scattered field are presented to illustrate the evolution of observed backscattering processes.

The empty and layered shells have almost the same decay pattern of the signals beyond the initial return. Also the shell with rings and the shell with internal structures only have closely the same decay pattern. The decay rate for the empty shell is 0.064dB/μsec. A similar decay rate is observed for the layered shell, that is 0.071dB/μsec. Decay rates for the ringed shell and internaled shell are smaller, they are 0.051dB/μsec and 0.045dB/μsec.

The distribution of the rings store energy and become the major source of radiation at later time. The internal structures also influence the radiation at later time. The rubber attachments of the internal structures limit the shell's radial motion to prefer two maximum and minimum ring motion. Therefore, the shell with internal structures and layered shell show dominant second ring frequency response.

Contents

1. Introduction

Acoustic scattering by four different cylindrical shells at normal incidence has been analyzed. The incident wave is a short transient, such that we can exclude the interference between the geometric field, which is initially scattered from the shell, and the radiation field caused by the induced elastic waves in the shell. Therefore, the scattering can be easily divided into the geometric field and the elastic field. The geometric field fills about the first 30 μsec of the scattering signal. It depends on the geometry of the shell and the basic properties of the shell like mass or elasticity of the shell. After the geometric field, the induced waves which travel through the shell and its internal structures influence the scattering process, until the whole energy received by the shell from the incident sound wave, is consumed and reradiated into the water. Therefore, the different properties and different structures of the shell make different contribution to the scattering in both the geometric field and elastic field.

This research is motivated by an interest in the acoustic properties of ship and submarine hulls. Internal structures are often resiliently mounted to the hull to inhibit the local transmission of the vibration energy from machinery and supporting structure to the hull. The presence of the resiliently mounted structures and structural discontinuities imposed by hull stiffeners must influence the acoustic scattering properties of the hull.

Experimental and analytic studies of the scatter generated by plane wave insonification of infinite cylindrical shells have been presented in a variety of references. The effect of induced elastic waves and the azimuthal dependence of the scattered field have been studied by Feit[1] and Marston[2,3]. Similar analytic studies of the plane wave scattering from infinite cylindrical shells at oblique incidence, and the influence of helical elastic waves, have been studied by Felsen and Ho[4,5,6]. There are a few experimental or analytical studies of acoustic scattering from finite cylindrical shells or internally loaded

shells. Maze et al [7] conducted experimental and theoretical studies of the influence of the resonant excitation of elastic waves on finite solid cylinders at normal and axial angles of incidence. Guo[8,9] has analytically studied the scattering effects of infinite cylinders internally loaded with two dimensional mass spring systems or elastic plates. Scattering from finite cylindrical shells with internal structures are studied by Corrado[10]. He conducted experimental studies of the scattering from three of the shells considered here; empty shell, ringed shell and internalled shell, for various angles of incidence. He also analytically studied scattering from a finite empty cylindrical shell, but with perfectly reflecting endcaps.

Scattering by a cylindrical shell in water is influenced by the induced dynamic interaction between the exterior shell and the internal structure. Comparing the scattering from the different shells helps us to understand and interpret the dynamics of the scattering process. In the empty shell case, many fundamental scattering processes that are common to the more complex shells are evident, and are more readily interpreted. In the shell with ring stiffeners, the stiffness of the shell is changed along with its mass, and provide discontinuities along the shell to axially propagating elastic waves. In the shell with internal structures, the role of the internal structures is added to the ring stiffened shell case. In the case of the layered shell, dissipation of the elastic waves along the shell by the damping material between the sandwich shell may decrease the effect of the axially traveling waves.

Shell designs are described in Chapter 2.

In Chapter 3, I study the lumped system response of infinitely long cylindrical shells. Such simple models are used to study the initial scattering by the empty shell, ring-stiffened shell and shell with internal structures. The stiffening rings and internal structures are simplified as a uniform mass load. The analytical results are not close to the experimental data. The stiffness changes by the distribution of the rings are not modeled

by the uniform mass load. Also the simplified spring, damper and mass model could not well model the internal structures. The uniform mass loading assumed decreases the initial scattering by the shell. But the mass connected to a shell by a spring and a damper does not influence initial scattering much.

The measured backscatter at beam aspect from the different shells are examined in Chapter 4. Both time and frequency domain representations are shown for the different shells; empty shell, ring-stiffened shell, shell with internal structures only and layered shell with the same internal structures. The internal structures change the basic scattering properties of the shell and increase the initial scattering about 2dB. This small influence of the internal structures is limited to the initial scattering. The elastic field decay rate for the layered shell is similar to that of empty shell for times less that 800 μsec. The rings and internal structures in the ring-stiffened shell and complex shell provide the additional energy storage. Therefore, the decay rates for these two shells are lower than those for empty shell and layered shell. Every shell has dominant scattering frequencies that relate to elastic resonance frequencies. Variations of these frequencies cause changes in the major scattering sources of the shell. Rings in the stiffened-ring shell, internalled shell and layered shell become the major source of the radiation. The shell itself is the major scattering source for the empty shell for all time, but for the others at later time, about after 60 μsec, the influence from the internal structures becomes dominant.

2. Shell Designs

The design parameters of the four shells are summarized in Table 2.1. See the Conti and Dyer [11] and Corrado [10] references for primary information on these designs. The design of the empty shell serves as the base exterior shell design for the other three shells. The basic shell dimensions are illustrated in Figure 2.1. The ring stiffened shell is comprised of the same exterior shell design configuration, but stiffened by four large nickel rings that are unequally spaced along the axis of the cylinder, as illustrated in Figure 2.1. The total mass of the rings equals the mass of the exterior shell, and they introduce structural impedence discontinuities to waves propagating on the shell. The internally loaded, complex shell was designed to provide a means of evaluating the effects of resiliently mounted wave bearing structures. The internal structures are supported from the rings of the stiffened shell, of the same configuration discussed above and illustrated in Figure 2.1. The internal structures consist of a quadrant symmetric arrangement of one inch diameter Delrin rods interconnected by cylindrical stainless steel masses as illustrated in Figure 2.2. The stainless steal masses are individually supported from the ring stiffeners by independent, triangular shaped rubber blocks made of EAR C1002 Isodamp rubber. The various internal components are all secured to one another with an epoxy compound. The total mass of the internal structures and ring stiffeners is approximately three times greater than the mass of the shell. In the layered shell, a rubber layer is sandwiched by the two concentric shells each 0.000532m thick, over the complex shell. The rubber material in this sandwich is 0.001m thick and also made of EAR C2206-03 Isodamp rubber.

Table 2.1 Summary of Model Design Parameters

Configulation	
Shell & Ring Material	Ni-200
Length Overall	0 86m
Shell Radius	0.05537m
Shell Thickness	0.000532m
Ring Thickness	0.01m
Ring Width	0.0125m
Mass Ratio, Rings/shell	1
Mass Ratio, Internals & Rings/Shell	3
Mass Ratio, Internals & Rings & Layer/Shell	4

Approx. Shell Material Properties		
Young's Modulus, E	2.2×10^{11}	N / m^2
Density, ρ	8900	kg / m^3
Poisson's Ratio, ν	0.31	
Compressional Plate Wave Speed	5270	m/s
Transverse Shear Wave Speed	3100	m/s

Approx. Delrin Material Properties		
Measured Dynamic Modulus, E	3.7×10^{9}	N / m^2
Density, ρ	1400	kg / m^3
Poisson's Ratio, ν	0.35	
Measured Compressional Speed of Rod	1625	m/s

Approx. Rubber Material Properties		
Measured Dynamic Modulus, E	5.0×10^{8}	N / m^2
Density, ρ	1289	kg / m^3
Poisson's Ratio, ν	0.28	

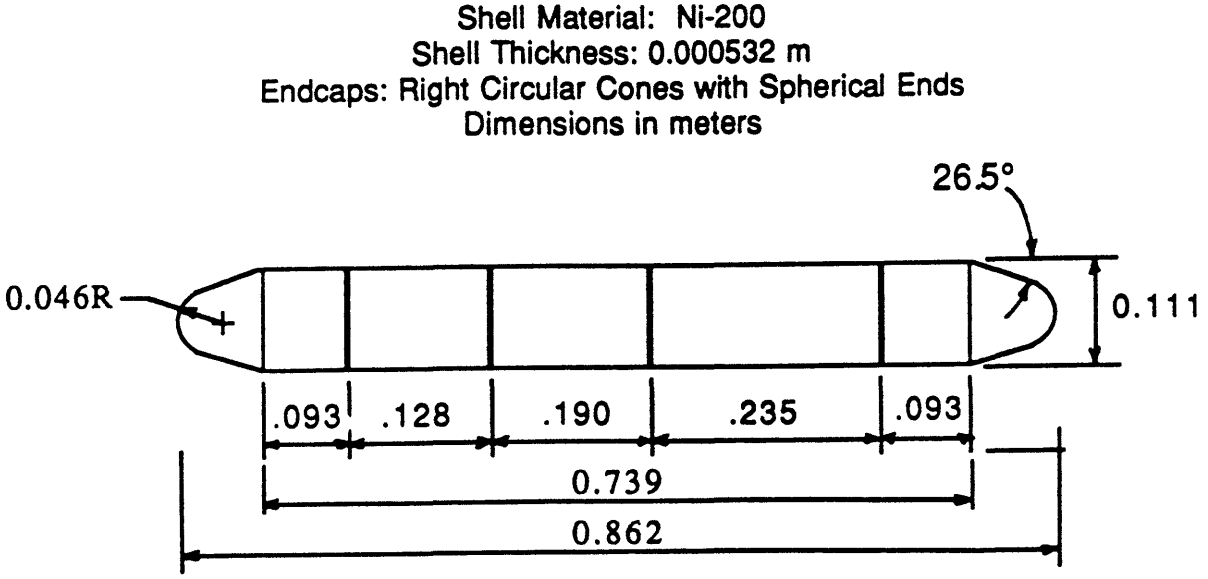

Figure 2.1 The Design Configulation of the Empty Shell Model and the location of the Ring Stiffeners (From C. Corrado)

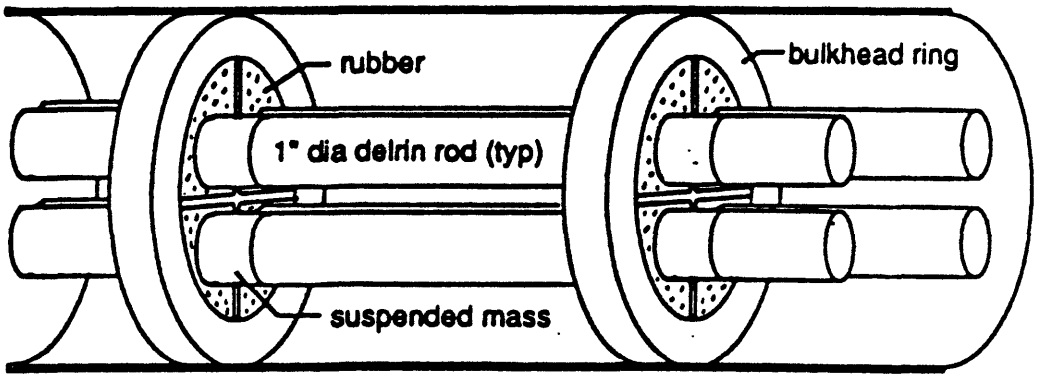

Figure 2.2 The Configulation of the Internal Structures (From M. Conti)

3. Dynamic response of infinite cylinders at beam incidence; lumped model

I have studied the initial or geometric scattering response of simplified models of the cylindrical shells. The initial return from the shell may depend only on simple properties of the shell, because the detailed dynamics of the shell mainly influence the scattering later in time. At beam incidence, radiation by the induced elastic waves can not affect the geometric return. Therefore, by studying a simplified model based on basic properties of the shell, we might understand the initial scattering process. The basic properties of the shell may include the geometry or structure of the shell, and its stiffness and mass.

I assume that the shells are continuous, infinitely long, cylindrical shells. Therefore, the effect of the elastic waves traveling along the axis of the cylinder is neglected. The empty shell is modeled by an infinite uniform cylinder. The masses of the rings are added to the infinite cylinder to model the ring-stiffened shell, by distributing them uniformly in the axial direction. Therefore, the structural impedance discontinuity along the shell is neglected. Also the stiffness increase by the ring distribution is not modeled well. For the shell with internal structures, the mass of the internal structures is included with a spring and damper model for the triangular shaped rubber blocks. The rubber block has many natural frequencies and many complex mode shapes.

A finite element method is used to find the natural frequencies and mode shapes of the rubber block. The two dimensional motion of the rubber block with the internal mass is analyzed. Figure 3.1 shows the lowest natural mode shape and the first 40 natural frequencies of the rubber block. The lowest natural frequency of the rubber block with the internal mass is ka=0.6. The damper has damping which is in inverse proportion to frequency. Figure 3.2 shows the diagrams for the shell with stiffened ring model and the shell with internal structure model.

I calculated the impulse response function for three of the four kinds of shells; empty shell , ring-stiffened shell and complex shell. The basic equations and formulations are shown in Appendix A. Figure 3.3 shows the Gaussian bandpass filter impulse response used in calculations, which is the same Gaussian filter used in experimental data analysis.

Magnitudes of the impedance functions, for a force F applied as in Fig 3.2, are shown in Figure 3.4. The extra masses affect the impedance function throughout the entire frequency range. The effect becomes larger after ka=2. The maximum impedance is shown at the resonance frequency of the spring/mass model in the internal shell case. After the maximum impedance, the impedance function of the shell with internal structure model becomes identical to the ring-stiffened shell model. Therefore, when the frequency is larger than the resonance frequency of the rubber block/internal mass system, the internal structure has no effect on the vibration of the shell. The impulse response function in Figure 3.5 shows that there are no differences between the ring-stiffened shell and the shell with internal structures. But there is a 30 % decrease of the impulse response from the empty shell case to the other two cases. The initial returns from the shells have a negative sense, and that is consistent with the pressure release cylinder.

The uniform mass loading of the rings and radiation inertia, which vibrates with the shell, creates the response decrease. But the mass of the internal structures does not influence the response. Because the impulse frequency band excludes the resonance frequency of the internal structures, hardly any energy can propagate through the spring to vibrate the internal structure. The impulse responses are calculated with different resonance frequencies of the internal structure. The impulse response return magnitudes are decreased as the resonance frequencies of the internal structures are increased. Figure 3.6 shows the impulse response function depends on the resonance frequencies of the internal structure. The simple spring and damper model can not contribute to the scattering much regardless of the resonance frequency of the model.

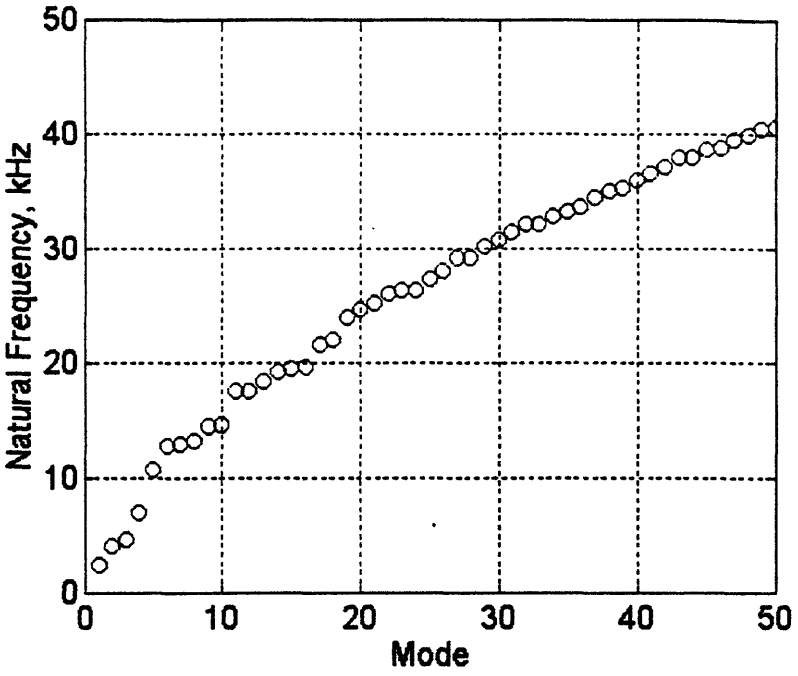

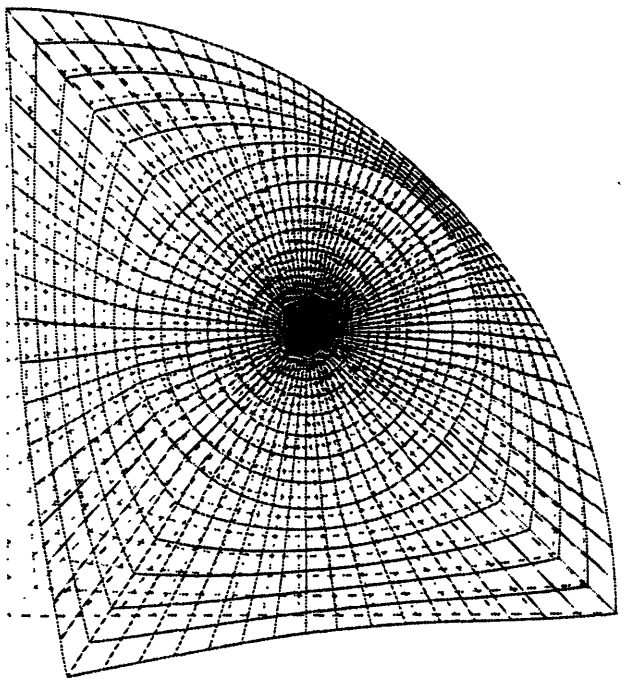

Fig 3.1 Natural frequencies of the rubber block with delrin and stainless steel mass inside. At 10kHz, ka=2.3.(up) Lowest natural modeshape for the rubber block with delrin and stainless steel mass inside. Motion is caused by a force acting on the arc, and parallel to the vertical axis.(down)

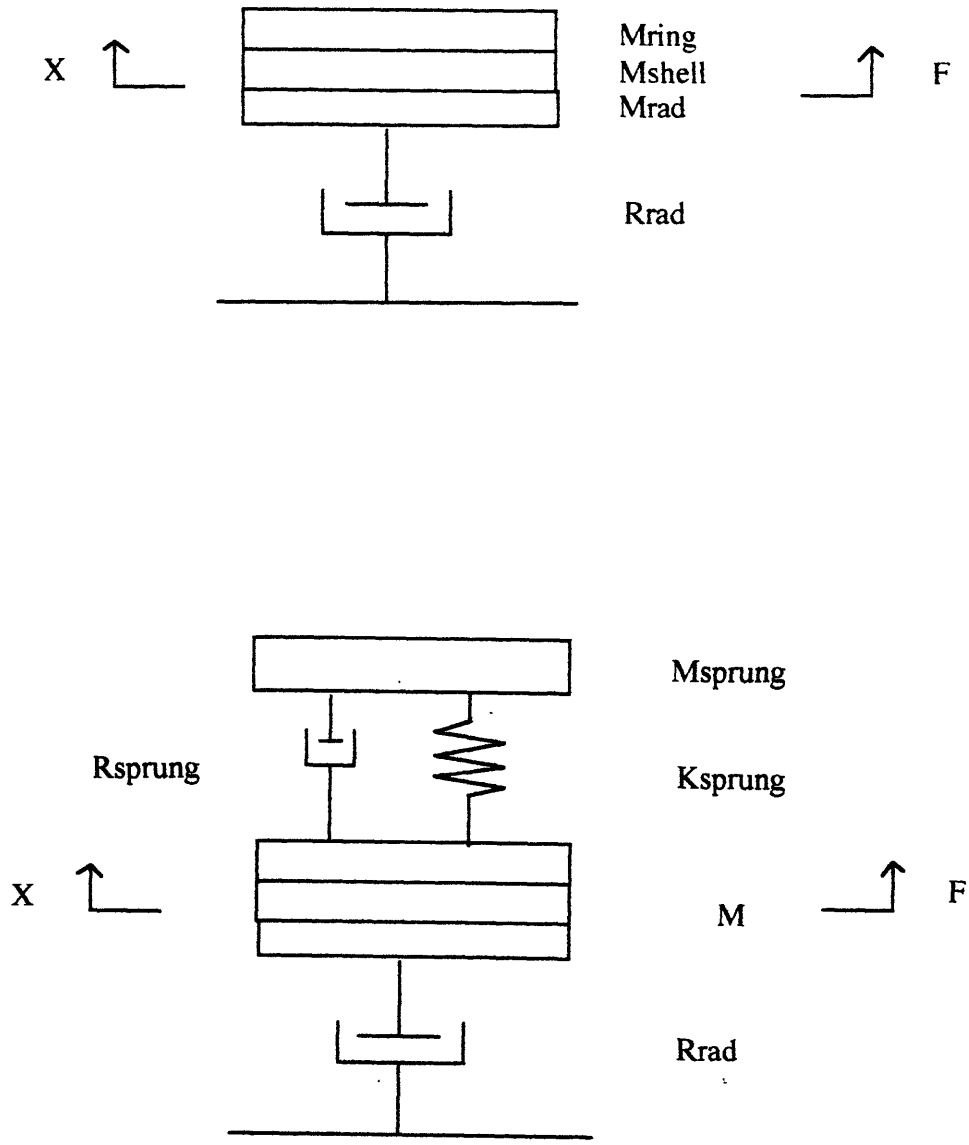

Fig 3.2 Diagram for Cylindrical Shell with Stiffening Rings (up). Cylindrical Shell with Internal Structures Model (down). The spring mass, sprirng and resistance refers to the sprung internal structures.

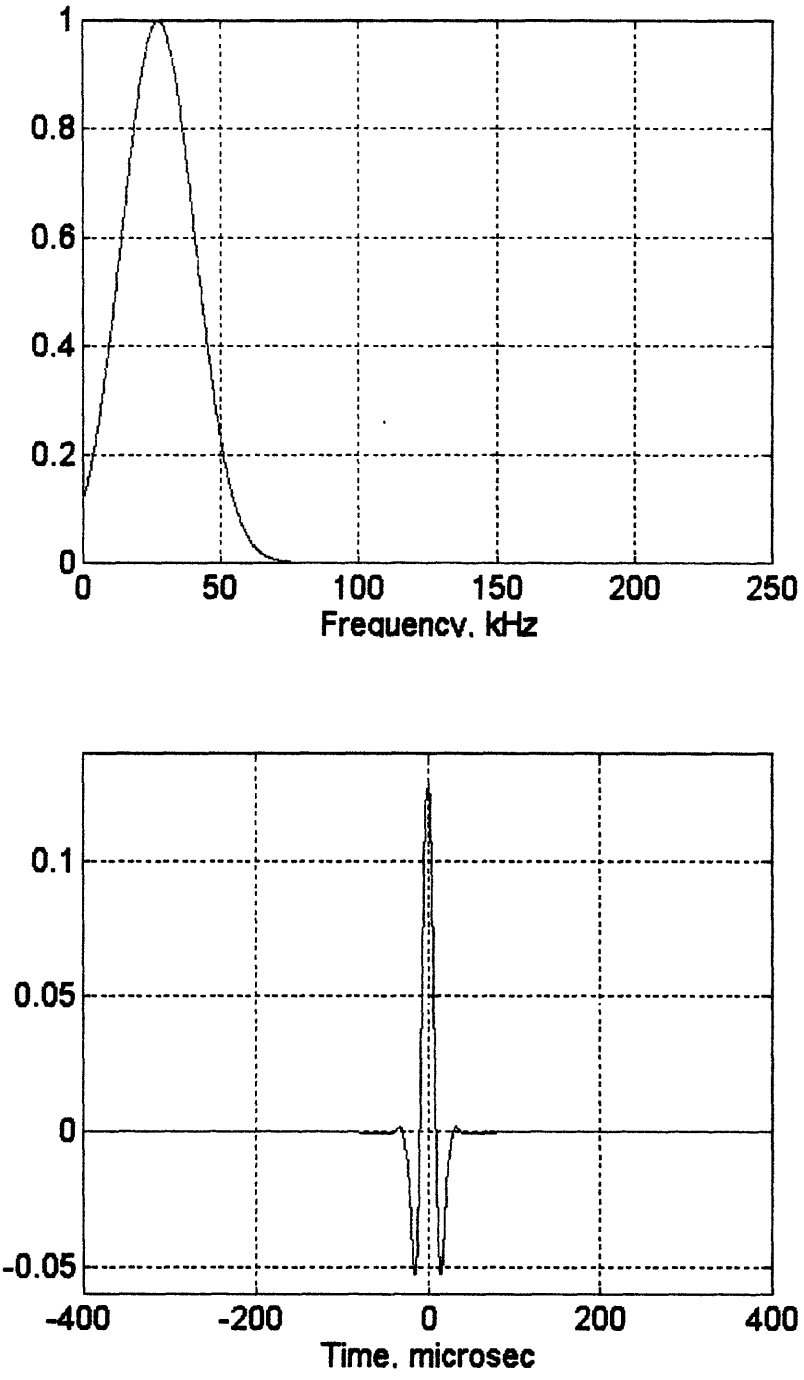

Fig 3.3 Gaussian Bandpass Filter (up), mean 27.3 kHz and standard deviation 13.2 kHz. Gaussian bandpass filter Impulse Response (Down), 6 dB down at Band Edges of the Frequency Range $2.75 < ka < 11.7$

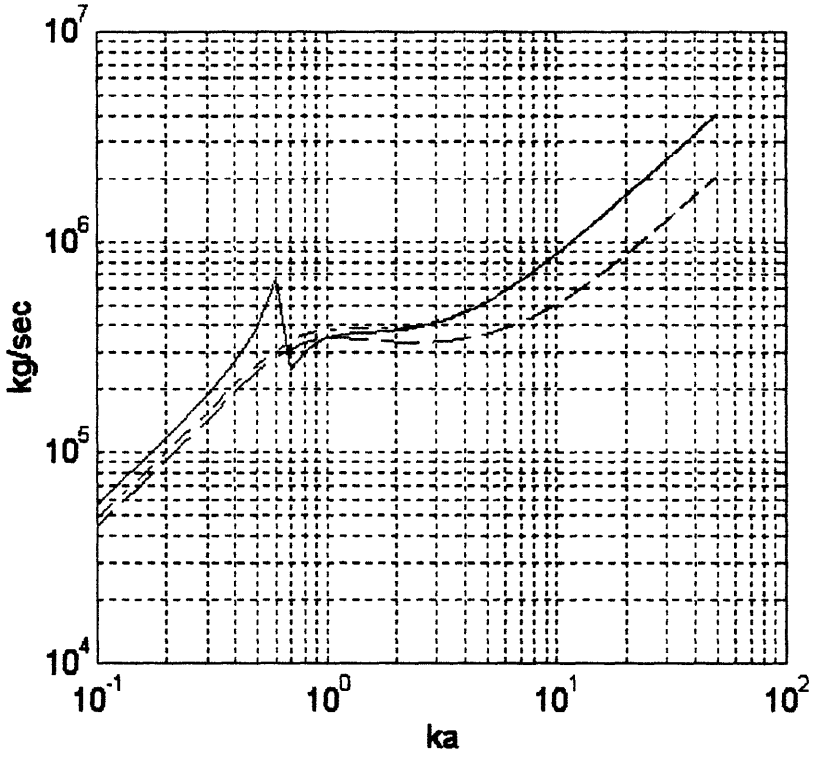

Fig 3.4 Magnitude of the Impedence Function for the three shell models (-- Empty shell, -. Shell with stiffening rings, - Shell with internal structures). These magnitudes are not filtered by the Gaussian function in Fig3.3.

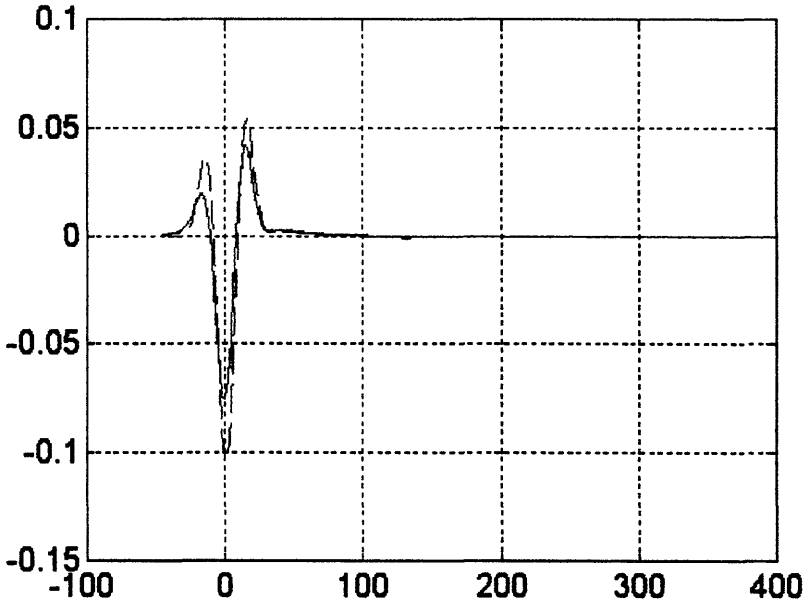

Fig 3.5 Gaussian bandlimited impulse response function of three shell models (-- Empty shell, -. Shell with stiffening rings, - Shell with internal structures)

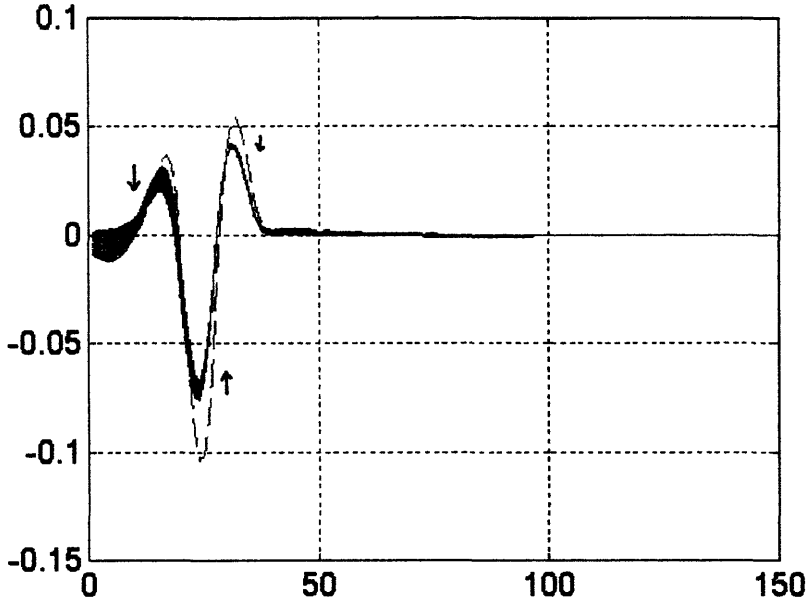

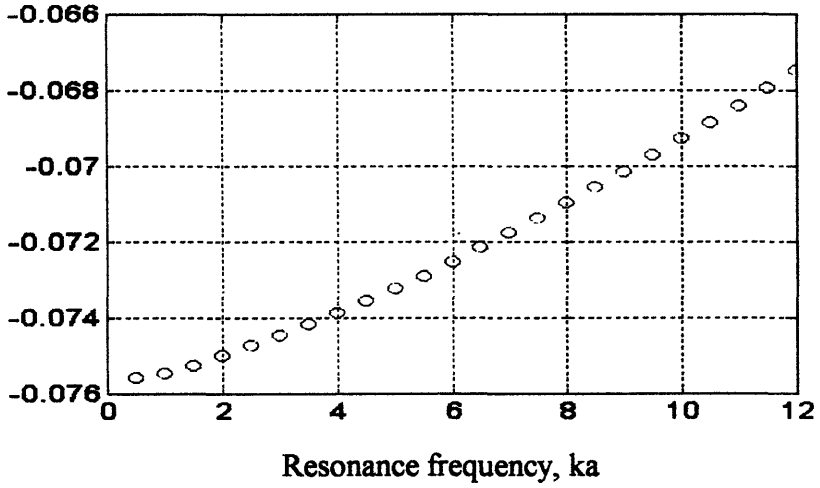

Fig 3.6 (Up) Bandlimited impulse response functions with increasing resonance frequency of the internal structure. Arrow shows the changing direction as the resonance frequency increases from ka=0.6 to ka=12. The break line shows the impulse response function for the empty shell. (Down) Maximum return in impulse response as the resonance frequency changes.

4. Sound scattering from the four different shells at beam incidence; analysis of measurements

4.1 Introduction

From the analytical calculation of a simple lumped approximation for an infinite shell, I have studied a few of the possible bases of scattering from the actual shell and how the mass affects the initial scattering. In the real experimental data analysis, we also have to consider the influence of the finiteness of the shell and axially traveling waves. The structural design differences of the shells also affect the sound scattering. Distribution of the rings and internal structures change the basic properties of the shells and influence the scattering process.

Beam incidence, monostatic sound scattering data are analyzed for each of the four shells.

4.2 Empty shell

In the empty shell, at least for beam incidence, we can consider this as a infinite shell only if the length of the cylinder is long enough. The waves on the shell, which are induced by the plane sound wave, propagate in the axial as well as circumferential direction. If the axial waves are damped out before they get back after they hit the end of the shell, we may consider this shell as an infinite shell.

The bandlimited impulse response of the empty shell at beam incidence is shown in Figure 4.2.1. This time domain representation of the scattering results from a deconvolution of the source signal from the scattered field measured at a radius of r=2m. The initial return from the shell has a negative sense that is consistent with a pressure release surface. After the geometric return, there are a series of returns which have a 62-66 μsec period. These are produced by radiation from the induced circumferential compressional wave and have an opposite sense with respect to the initial return. The radiation losses that occur as the induced compressional wave circumnavigates the shell, are partially the cause for the observed decay. The logarithm of the magnitude of the analytic signal representation of the backscattered signal is shown as a function of time in Figure 4.2.2. I have used this representation to calculate the decay rate of the backscattered signal. A least squares linear fit of the envelope yields a broadband amplitude decay rate of 0.064 dB/μsec. In this calculation I exclude the initial return and the returns that are less than -75dB, as the latter could include noise.

Figure 4.2.4 shows the same analysis as in Figure 4.2.2 but in different frequency bands. I used three partially overlapping Gaussian windows to observe the decay rate of signal returns depending on the frequency band. Each window is shown in Figure 4.2.3. I choose the low frequency band from 10kHz to 24kHz ($2.35 < ka < 5.64$), the mid frequency band from 20kHz to 34kHz ($4.70 < ka < 7.99$), and the high frequency band from 30kHz to 44kHz ($7.05 < ka < 10.34$). In each band, the decay rates are same, and are about 0.063dB/μsec. At beam incidence the transverse shear waves propagate with no radial displacement component and do not contribute to the scattering. The decay of the returned signals is partially caused by the radiation losses as the compressional wave circumnavigates the shell. So these radiation losses do not depend on the frequencies. But because the rate is so much smaller than the theoretical radiation loss rate of 0.089dB/μsec,we must consider that the energy is partially stored in the finite shell, no doubt due to induced compressional axial waves[12].

The speeds of the poorly radiated flexural waves are not fast enough to travel all the way to the end of the shell. In the frequency bands I used, the time it takes for flexural waves to travel the entire shell is 3200 - 1600 μsec depending on the frequency. So the signal returns for the empty shell are only caused by the induced compressional waves. These induced compressional waves have to have specific periods and frequencies to fit into the shell circumference. The first ring frequency is 15kHz with a 66μsec period. The second ring frequency is 30kHz with a 33μsec period. The magnitudes of the spectral function from the Fourier transform of the bandlimited impulse response are shown in Figure 4.2.5. To exclude the initial return, the first 30μsec of the data are excluded. In the empty shell case, after 800μsec, the signals are too small to consider as a scattering signal from cylinder. So the data after 800μsec are excluded. Figure 4.2.5 shows the dominant frequency responses to be at the first and second ring frequencies. The analysis for the total time has the shape of the Gaussian bandpass filter, except for the dominant responses near the first and second ring frequencies. This shape disappears as the analysis goes to the later time.

For the empty shell, the induced compressional waves mostly control the scattering process after the geometric return. In our frequency band, the first and second ring frequency waves are mostly acting throughout the scattering process. The decay rate is determined only partially by the radiation loss during these compressional waves circumnavigating the shell, since the measured values are only about 70% of the theoretical decay rate.

4.3 Shell with stiffening rings

In the case of the shell with stiffening rings, the axial wave motion can affect the scattering more strongly. The induced flexural waves do not influence the scattering process of the empty shell, because flexural waves are too slow for the overall length. In the ring-stiffened shell, these flexural waves propagate to the rings, interact with rings, and radiate. The time it takes to excite the shortest bay can be calculated by the round trip travel time for flexural waves. I used flexural wave group speeds in a plate of the same thickness of the shell to calculate the round trip time. The round trip time is about 350μsec at a frequency of 27 kHz. So I expect that scattering by the shell itself may be dominant before 350μsec. The scattering by the rings, which are exited by induced compressional and flexural waves between the rings, may be the major effect on the scattering process after 350μsec.

The bandlimited impulse response is shown in Figure 4.3.1. The geometric return is about same as for the empty shell. But the elastic response after the initial return lasts longer than that of the empty shell. Figure 4.3.2 shows the logarithm of the magnitude of the analytic signal representation of the bandlimited impulse response. I extract two decay rates. The first decay rate of 0.051dB/μsec is calculated from the first 350μsec of the signal. This is the decay rate before the flexural wave can excite the shortest bay. The signal after 350μsec has a 0.011dB/μsec decay rate. Therefore, after the bays are exited, the decay rate is decreased to one fifth. But even before one of the bays being excited, the decay rate is still smaller than the empty shell case. This is so because the rings can be the energy transfer mechanism during this time.

Figure 4.3.3 shows the logarithm of the magnitude of the envelope of the three different frequency bandlimited impulse responses. I extracted the decay rates for these frequency bands. Because the flexural waves are dispersive, the time it takes for the flexural waves to excite the shortest bay is different for each frequency band. Before the flexural waves excite the shortest bay, the decay rates are 0.030dB/μsec for the low frequency band, 0.056dB/μsec for the mid frequency band and 0.085dB/μsec for the high

frequency band. After the flexural waves excite the shortest bay, which are after 450 μsec for low frequency band, after 350 μsec for the mid frequency band and after 250 μsec for the high frequency band, the decay rates decrease remarkably. These are 0.0032dB/μsec for the low frequency band, 0.0066dB/μsec for the mid frequency band and 0.0114dB/μsec for the high frequency band. These decay rates increase as the frequency band goes higher. Compared to the empty shell case, which have the same decay rates for all three frequency bands, the decay rates for the shell with stiffening rings case depend on the frequency band.

In the shell with stiffening rings, the early decay rates are smaller than the empty shell. Hence, the ring stiffeners and the bays between them must provide the energy storage mechanisms to decrease the radial amplitude at the shell exterior. And at later time, the rings and bays radiate the stored energy.

Magnitudes of the spectral function of the bandlimited impulse response function are shown in Figure 4.3.4 and Figure 4.3.5. The Fourier analysis of the first 30μsec to 350μsec signal is shown in Figure 4.3.4 (a). The break line shows the Gaussian bandpass filter that can be interpreted as the spectral function for the input impulse signal. The Fourier analysis of the first 350μsec response has the shape of the input signal. Figure 4.3.4 (b) shows the magnitude of the spectral function for the 350μsec to 1200μsec response signal. These still reflect the shape of the input signal.

Figure 4.3.5 shows the magnitude of the spectral function of the bandlimited impulse response for different time periods. The spectral density for the 30μsec to 1200μsec response has peaks near 17kHz, 22kHz and 31kHz, the first and third of which may correspond to the first and second ring frequencies. But these frequencies, if they are the ring frequencies, are shifted a little to higher frequencies compared to the empty shell case. These frequency shifts, especially for the second ring frequency, are more noticeable especially when the first 100μsec or 200μsec response signals are excluded as shown in

figure (b) and (c). The shifted ring frequencies, especially evident at t>100μsec, indicate that the main scattering sources are moved from the shell to the rings. Because the mean circumference of the rings is smaller than that of the shell, the induced compressional waves traveling through the rings have higher ring frequencies than those of the shell. The mean ring radius is 9% smaller than the shell radius, and can easily account for the observed values. But the 22kHz peak has no ready explanation. Nonetheless, the agreement of the prediction with the measurement at 17 and 31kHz suggests quite strongly that these are indeed related to ring motion.

When the shell with stiffening rings is insonified by the plane wave, first the induced compressional waves, which circumnavigate the shell, are the main source for the scattering. After axial flexural waves reach the rings the scattering from the rings becomes the dominant scattering process. Therefore, the ring frequencies are more readily observed in the spectral function of the response for the later time, as we have seen in Figure 4.3.5.

4.4 Shell with Internal Structures

The internal structures of the shell may provide additional energy storage for the scattering process. The interaction with the internal structures might be frequency dependent. Figure 4.4.1 shows the natural frequencies of the internal structures. These natural frequencies are analytically calculated. The longitudinal and flexural coupled motions in the derlin rods connected to stainless steel masses are considered in this analysis. The analysis, summarized in Appendix B, shows that the modal density of the internal structures in our frequency band is high, and we can consider that the internal structures respond through the entire frequency range.

The bandlimited impulse response of the shell with the internal structures is shown in Figure 4.4.2. There is about 25% increase in amplitude of the first return(about 1.9 dB) compared to the empty shell case. Thereafter, the responses become more complicated than the shell with stiffening ring case. But the decay rates from the logarithm of the magnitude of the analytic signal representation (Figure 4.4.3) are 0.045 dB/μsec for the first 350 μsec and 0.0081 dB/μsec for the time after 350 μsec, and are similar to those from the shell with stiffening rings. The decay rates for the different frequency band are shown in Figure 4.4.4. The decay rate increases when it goes from the low frequency band to the mid and high frequency bands. These rates are 0.032 dB/μsec for the low frequency band, 0.078 dB/μsec for the mid frequency band, and 0.076 dB/μsec for the high frequency band. The decay rate seems to be unchanged when it goes from mid to high frequency. After the flexural wave transition, the bays, which are excited by the flexural waves, influence the scattering, with decay rates of 0.0011 dB/μsec, 0.0108 dB/μsec and 0.0087 dB/μsec. These increase from low to mid and high frequencies, although the high frequency value is somewhat smaller than the mid frequency one.

The magnitude of the spectral function from the Fourier analysis of the 30 μsec to 350 μsec signals are shown in Figure 4.4.5(a). The spectral function of the first 350 μsec signal has the shape of the Gaussian input spectral function. But the spectral function of the later time signals, as shown in Figure 4.4.5 (b), does not have the Gaussian shape any more. It is more like a constant response versus frequency.

Figure 4.4.6 shows the magnitude of the spectral function from the Fourier analysis of the different time periods of the bandlimited impulse response. Figure (a) shows the spectral density of the 30 μsec to 1400 μsec signal. It shows the first ring frequency at 17kHz and the second at around 31kHz. The 22kHz component noted for the ring stiffened shell, is now more diffusely seen as a broader peak from about 20 to 26kHz. When I exclude the first 100 μsec of the signal, which is Figure (b), the first and the second ring frequencies are more noticeable. Also, the response at the second ring

frequency is bigger than the response at the first ring frequency. The 20 to 26kHz broad peak is notably absent in this time domain, while it was observed(as a narrower peak) for t>100μsec in the ring stiffened shell. The internal structures are attached to the shell by four rubber block elements, and have quadrant symmetry. These four attachments provide a reaction at the rings that guides their radial motion to the second ring frequency. After 200 μsec, the spectral response function is generally spread uniformly in frequency.

The internal structures do not seem to influence the decay rates greatly. Thus they provide at most small additional energy storage for the scattering process, but they spread the energy more uniformly throughout the frequency band. And the way the internal structures attach to the shell restricts the shell's radial motion. Therefore, the radial motion of the shell prefers the second ring frequency, which has two maximum and two minimum radial displacements along the shell's circumference.

4.5 Layered shell

In the layered shell, damping along the shell makes the scattering process much like the empty shell, at least for t<350μsec. The elastic waves, which travel through the shell surface to the rings, are now damped by the rubber layer between the sandwich shell. Therefore, the rings and internal structures are hardly excited at early times by the induced waves along the shell and could not influence the early radiation process.

The bandlimited impulse response and logarithm of the magnitude of the analytic signal representation are shown in Figure 4.5.1 and Fig 4.5.2. Only the first return is similar to the shell with internal structures only. But after that the signals are much like the empty shell case. The initial decay rate is 0.071 dB/μsec, which is similar to that of the

empty shell. But damping along the shell probably increases the decay rate for t>350μsec compared to that of the empty shell. Envelope functions for the different frequency bands are shown at Figure 4.5.3. The decay rates are calculated from the peak signals greater than -76dB. They are 0.044 dB/μsec for the low frequency band, 0.061 dB/μsec for the mid frequency band and 0.052 dB/μsec for the high frequency band. That varying decay rates depend on frequency indicates that the damping, as well as the elastic process, may depend on frequency.

The magnitudes of the spectral function of the impulse response are shown in Figure 4.5.4 and Figure 4.5.5. In the period 350 μsec to 1200 μsec, the magnitude of the spectral function shows maxima around the first and second ring frequencies, (although the second ring frequency is at 27kHz instead of 30 kHz). This indicates that the radiation by the induced compressional waves on the shell still has a major effect on the scattering process. Unlike the internal structures only case, the internal structures in the layered shell have little influence on the scattering energy even in this later period. But Figure 4.5.5 shows that the second ring frequency dominates the first ring frequency in all frequency bands. The four rubber block attachments influence the induced compressional waves to prefer second ring frequency radial motion, due to the quadrant symmetry of the internal structures.

The damping layer causes scattering from the layered shell to be similar to the scattering from the empty shell, for t<300μsec. In this time domain, rings and internal structures do not store enough energy to contribute to the scattering. But, the four rubber attachments causes second ring frequency radial motion of the shell to be dominant at later times. Damping along the shell increases the decay rate at later times to 0.032dB/μsec which is larger by about a factor of 4 than that of the internalled shell. This effect depends on frequency.

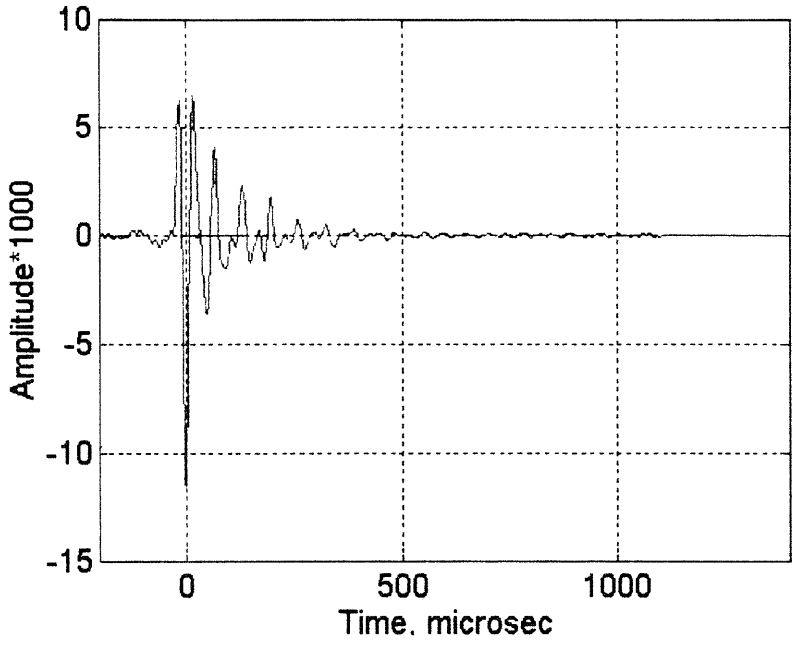

Fig 4.2.1 Measured Gaussian Bandlimited Monostatic Impulse Response of the Empty Shell at Beam Aspect for a Frequency Range 2.75 < ka < 10.0 and a Radial Distance of r=2m from the Target Center, normalized by the amplitude of the incident wave.

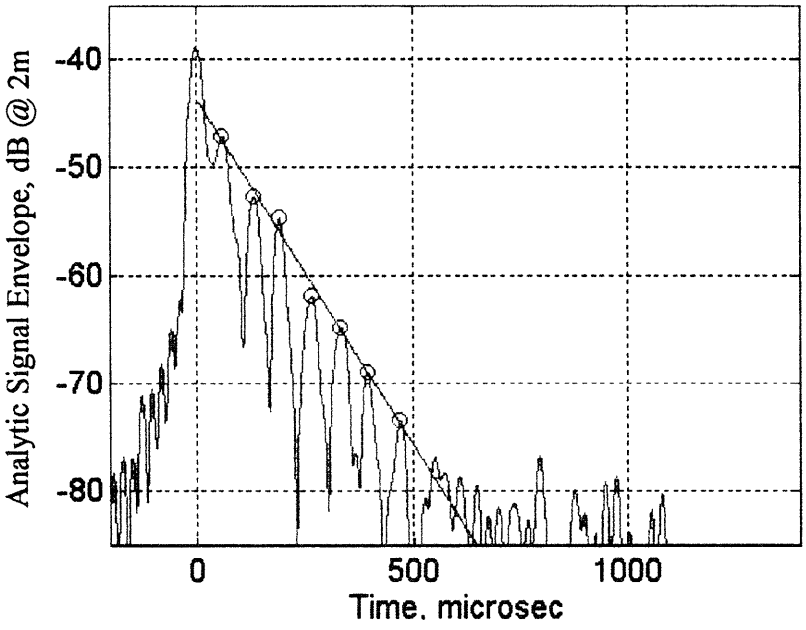

Fig 4.2.2 Logarithm of the Magnitude of the Envelope of the Gaussian Bandlimited Impulse Response of the Empty Shell at Beam Aspect, 2.75 < ka < 10.0 (Envelope is from Fig 4.2.1).

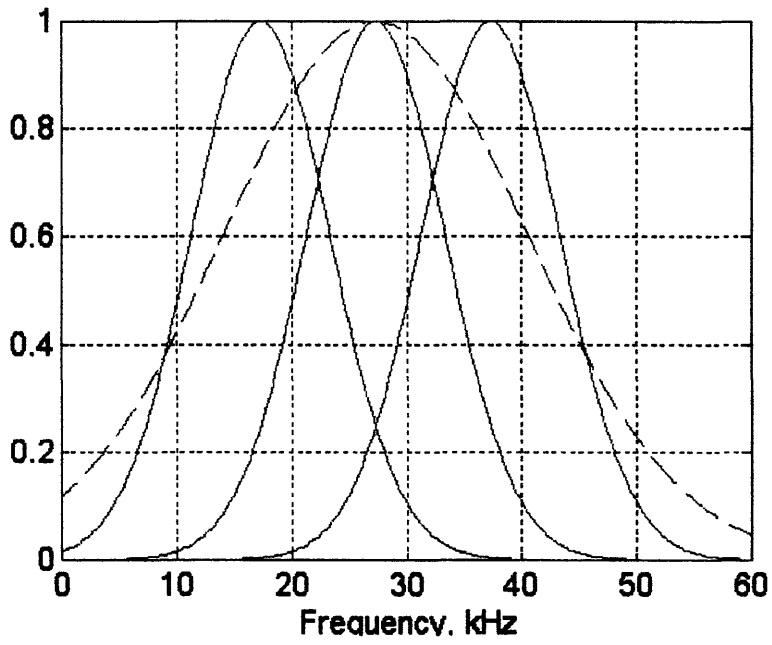

Fig 4.2.3 Gaussian Bandpass Filters, Low Bandpass Filter, 2.35 < ka < 5.64. Mid Bandpass Filter, 4.70 < ka < 7.99. High Bandpass Filter, 7.05 < ka <10.34. The dash curve is the overall Gaussian Filter

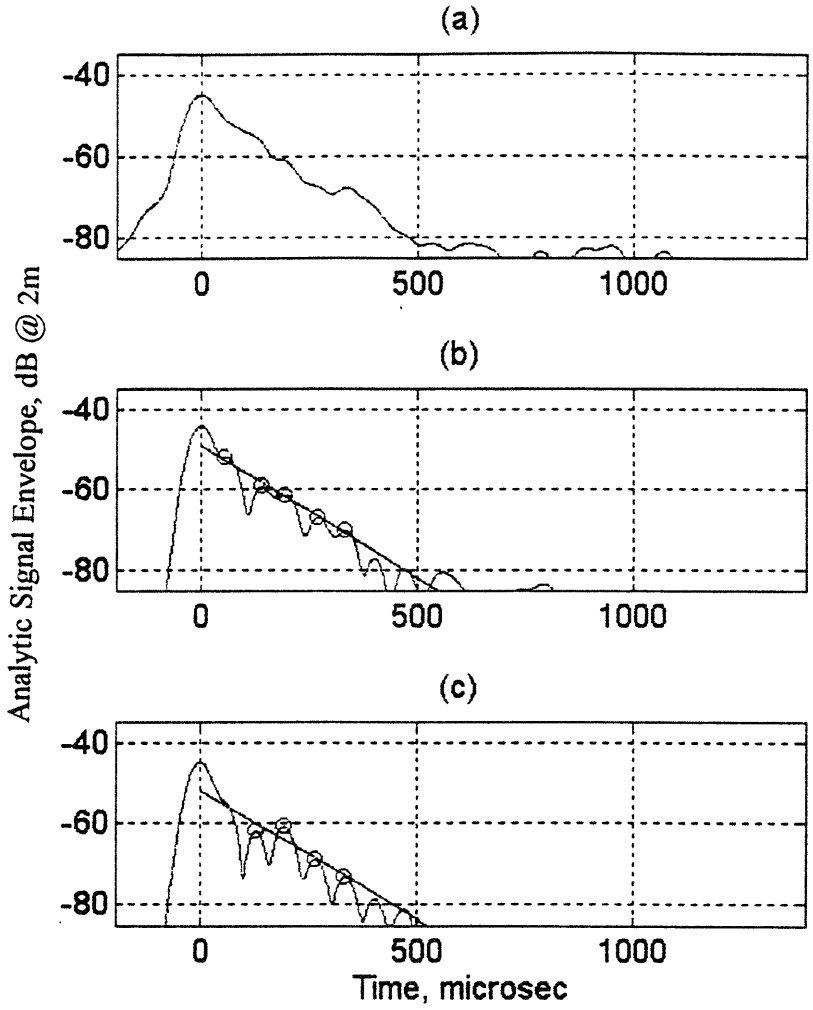

Fig 4.2.4 Logarithm of the Magnitude of the Envelope of the (a) Low Frequency Bandlimited Impulse Response (2.35 < ka < 5.64), (b) Mid Frequency Bandlimited Impulse Response (4.70 < ka < 7.99), (c) High Frequency Bandlimited Impulse Response (7.05 < ka <10.34), for Empty Shell at Beam Aspect

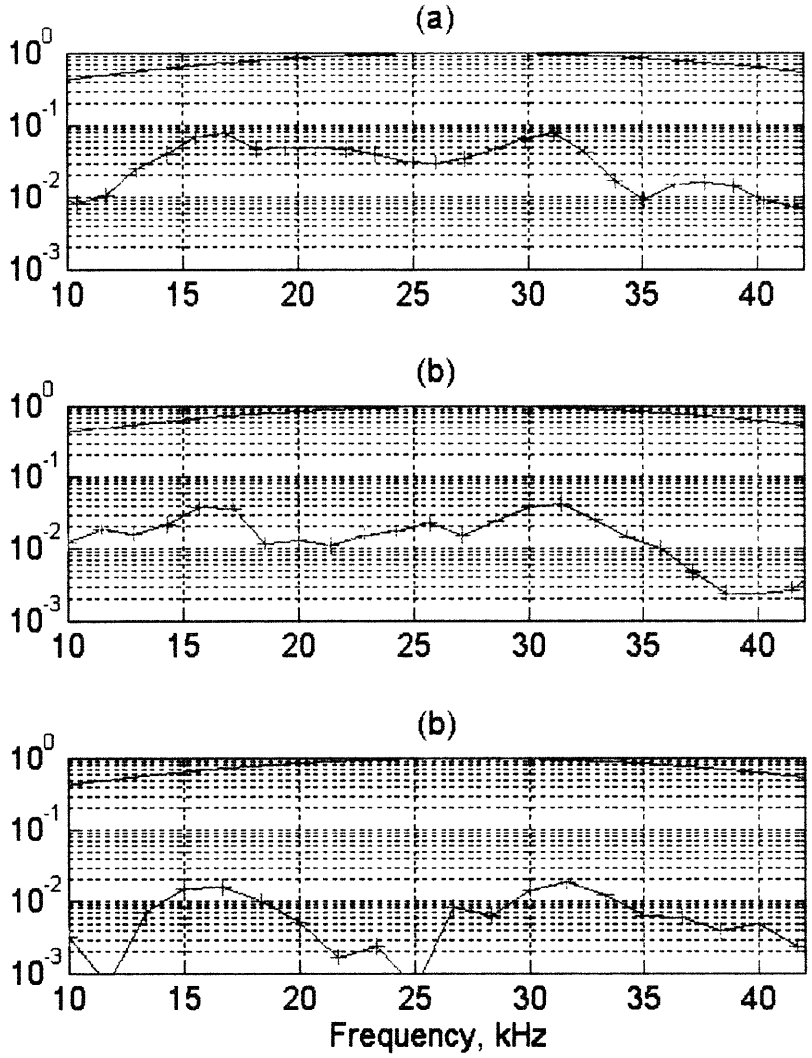

Fig 4.2.5 Magnitude of the Spectral Function of the Bandlimited Impulse Response of the Empty Shell at Beam Aspect for the period. (a) 30 μsec < t < 800 μsec, (b) 100 μsec < t < 800 μsec, (c) 200 μsec < t < 800 μsec. Broken line shows the Gaussian Bandpass Filter response.

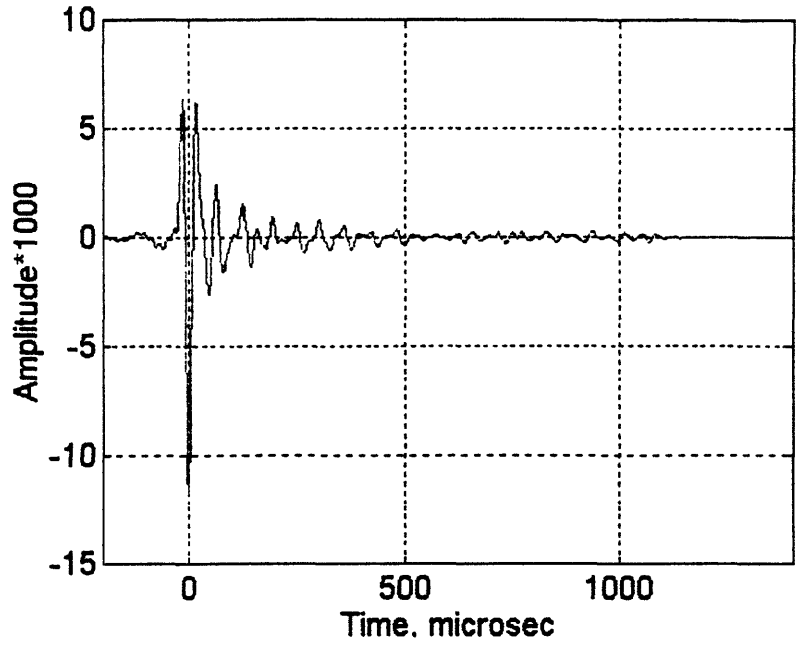

Fig 4.3.1 Measured Gaussian Bandlimited Monostatic Impulse Response of the Shell with Stiffening Rings at Beam Aspect for a Frequency Range 2.75 < ka < 10.0 and a Radial Distance r=2m from the Target Center.

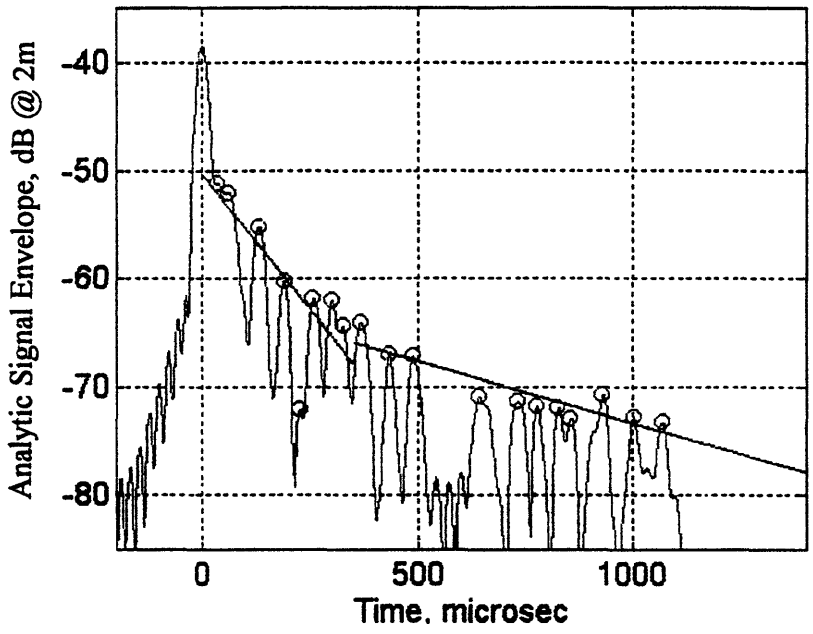

Fig 4.3.2 Logarithm of the Magnitude of the Envelope of the Gaussian Bandlimited Impulse Response of the Shell with Stiffening Rings at Beam Aspect.

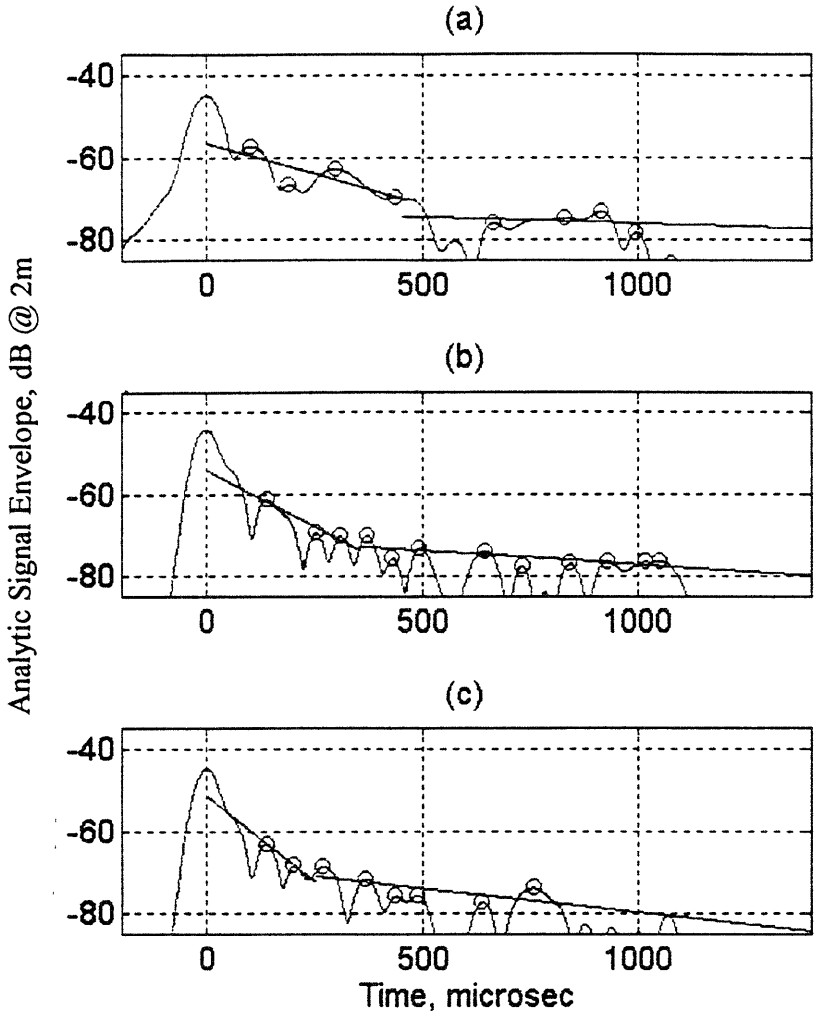

Fig 4.3.3 Logarithm of the Magnitude of the Envelope of the (a) Low Frequency Bandlimited Impulse Response (2.35 < ka < 5.64), (b) Mid Frequency Bandlimited Impulse Response (4.70 < ka < 7.99), (c) High Frequency Bandlimited Impulse Response (7.05 < ka <10.34), for Shell with Stiffening Rings at Beam Aspect.

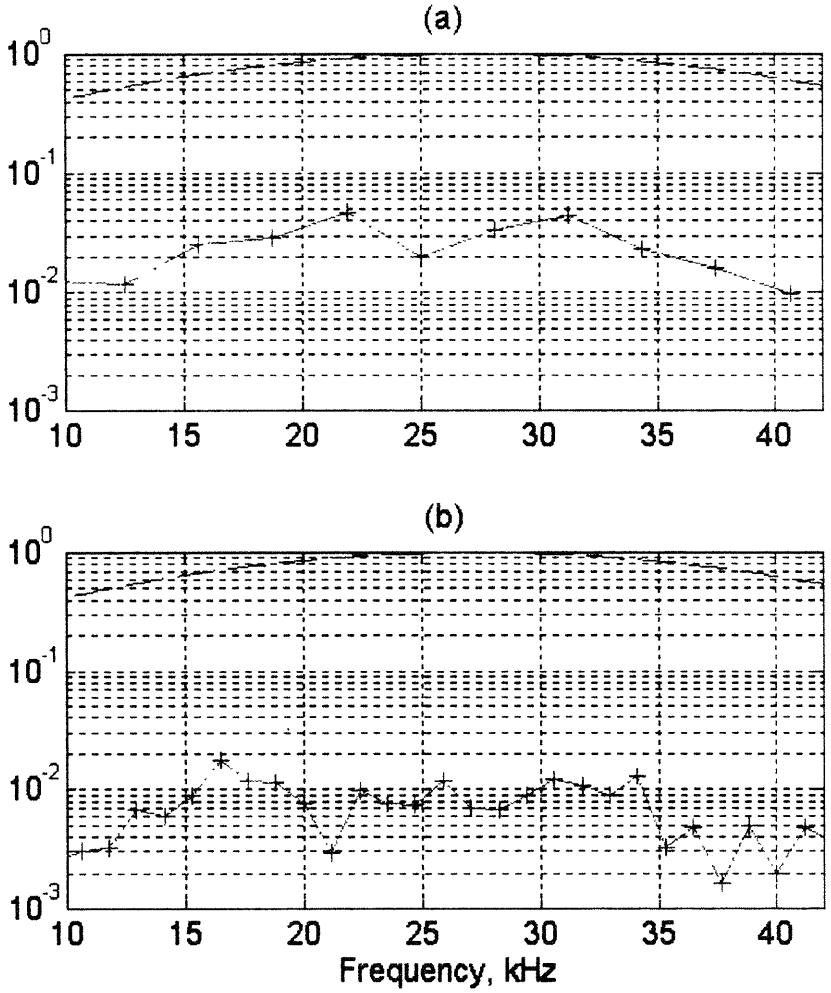

Fig 4.3.4 Magnitude of the Spectral Function of the Bandlimited Impulse Response of the Shell with Stiffening Rings for the time (a) 30 μsec < t < 350 μsec, (b) 350 μsec < t < 1200 μsec; break line shows the Gaussian Bandpass Filter.

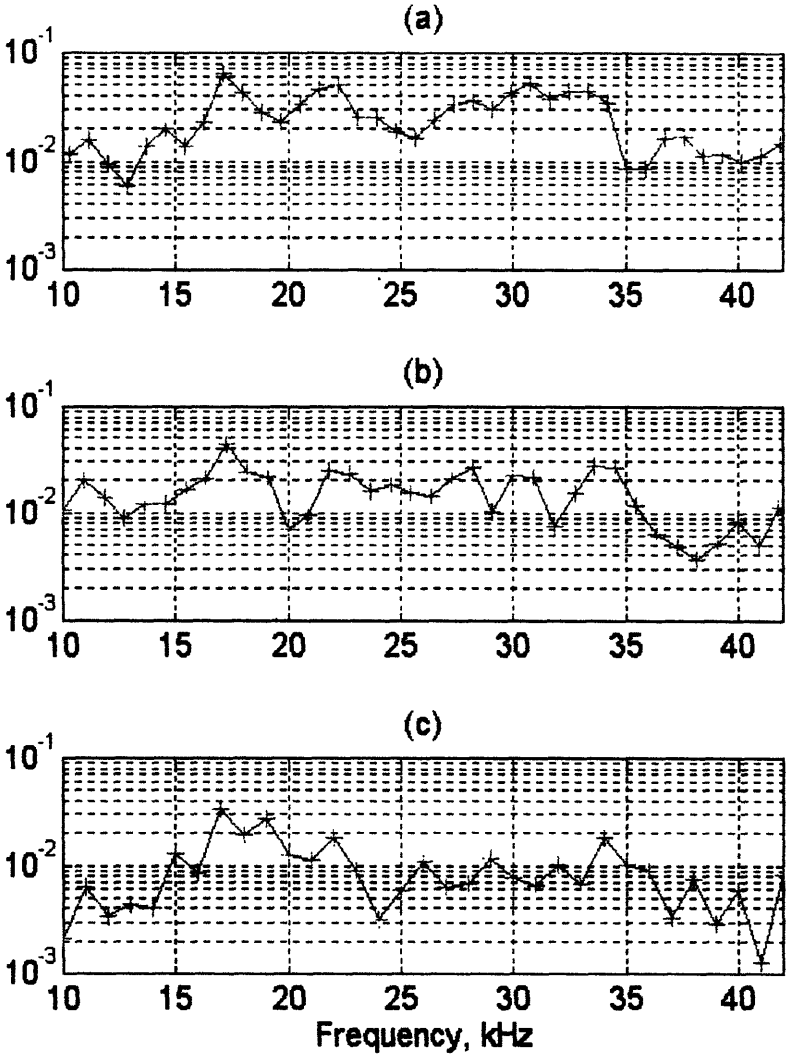

Fig 4.3.5 Magnitude of the Spectral Function of the Bandlimited Impulse Response of the Shell with Stiffening Rings at Beam Aspect for the period (a) 30 μsec < t < 1200 μsec, (b) 100 μsec < t < 1200 μsec, (c) 200 μsec < t < 1200 μsec

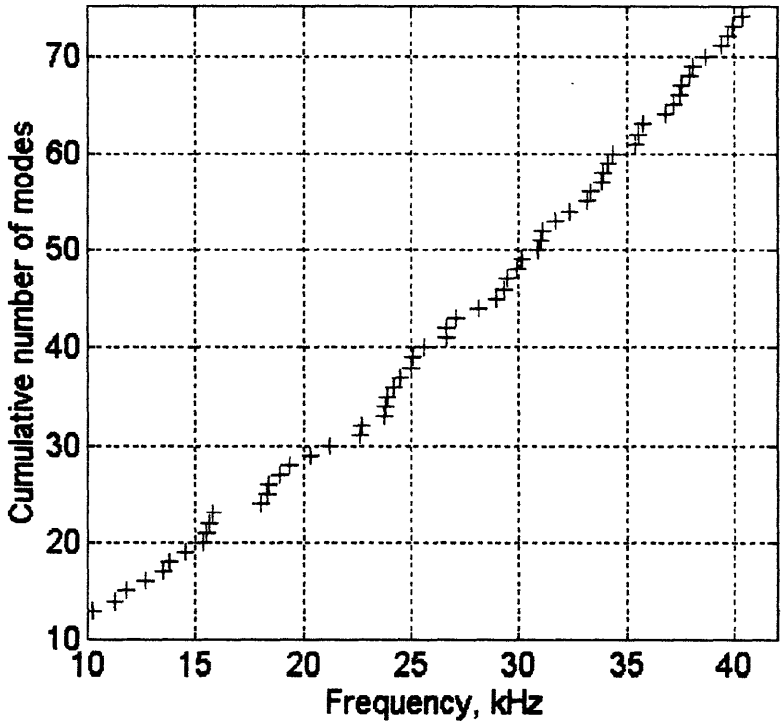

Fig 4.4.1 Calculated Natural Modes of the Internal Structure (There are 62 natural modes in the frequency range 10 kHz to 42 kHz)

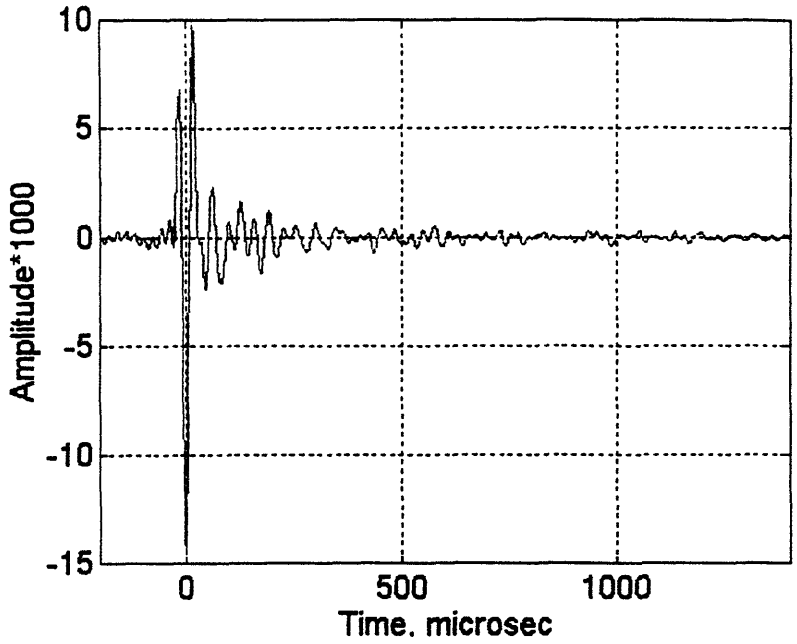

Fig 4.4.2 Measured Gaussian Bandlimited Impulse Response of the Shell with Internal Structure at Beam Aspect for a Frequency Range 2.75 < ka < 10.0 and a Radial Distance of r=2m from the Target Center.

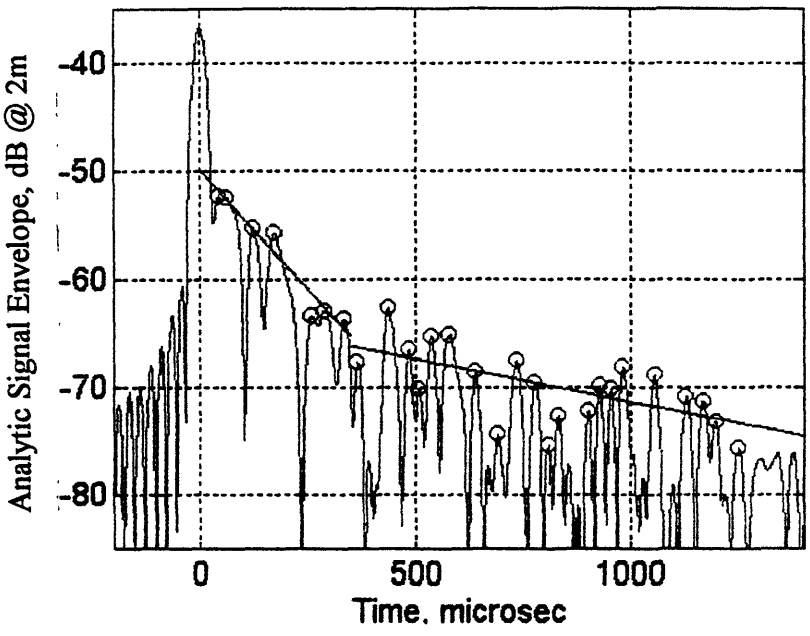

Fig 4.4.3 Logarithm of the Magnitude of the Envelope of the Gaussian Bandlimited Impulse Response of the Shell with Internal Structure at Beam Aspect.

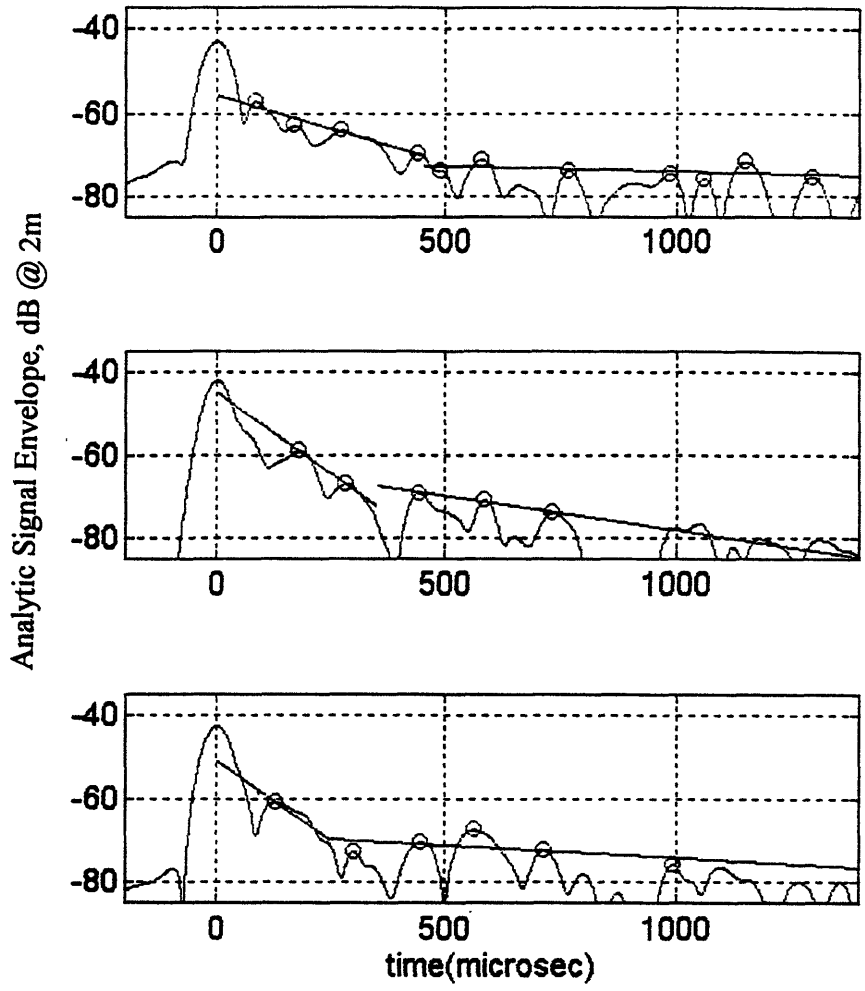

Fig 4.4.4 Logarithm of the Magnitude of the Envelope of the (a) Low Frequency Bandlimited Impulse Response (2.35 < ka < 5.64), (b) Mid Frequency Bandlimited Impulse Response (4.70 < ka < 7.99), (c) High Frequency Bandlimited Impulse Response (7.05 < ka <10.34), for Shell with Internal Structures at Beam Aspect.

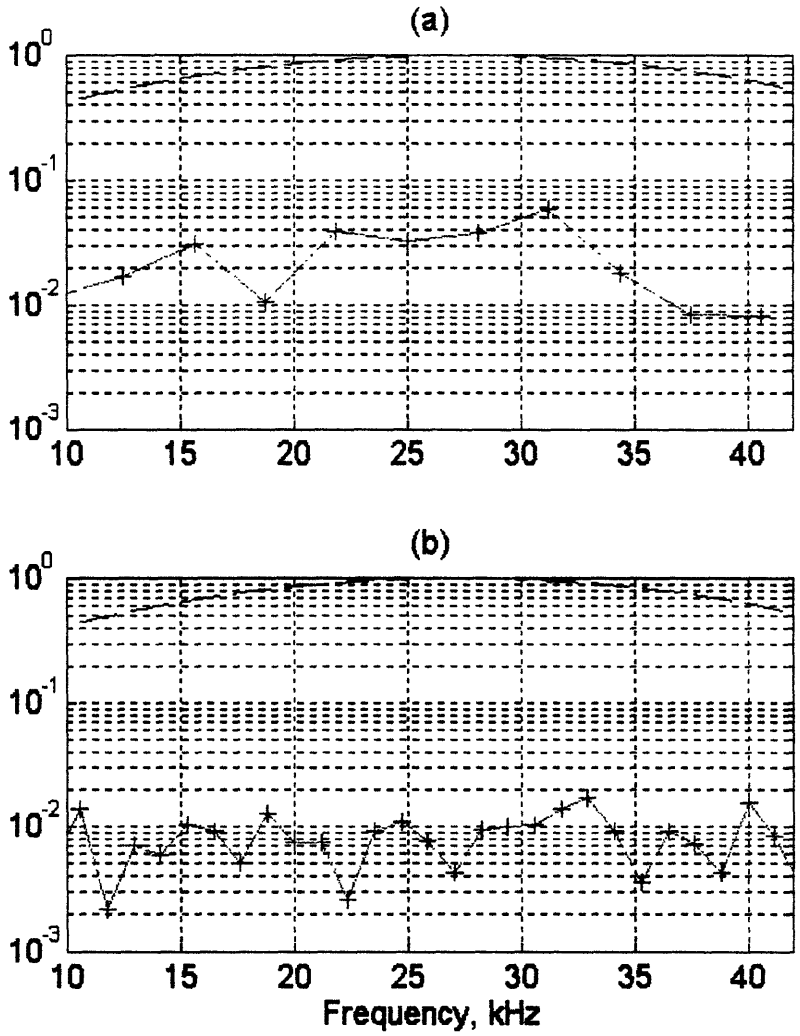

Fig 4.4.5 Magnitude of the Spectral Function of the Bandlimited Impulse Response of the Shell with Internal Structures for the period (a) 30 μsec < t < 350 μsec, (b) 350 μsec < t < 1200 μsec; break line shows the Gaussian Bandpass Filter

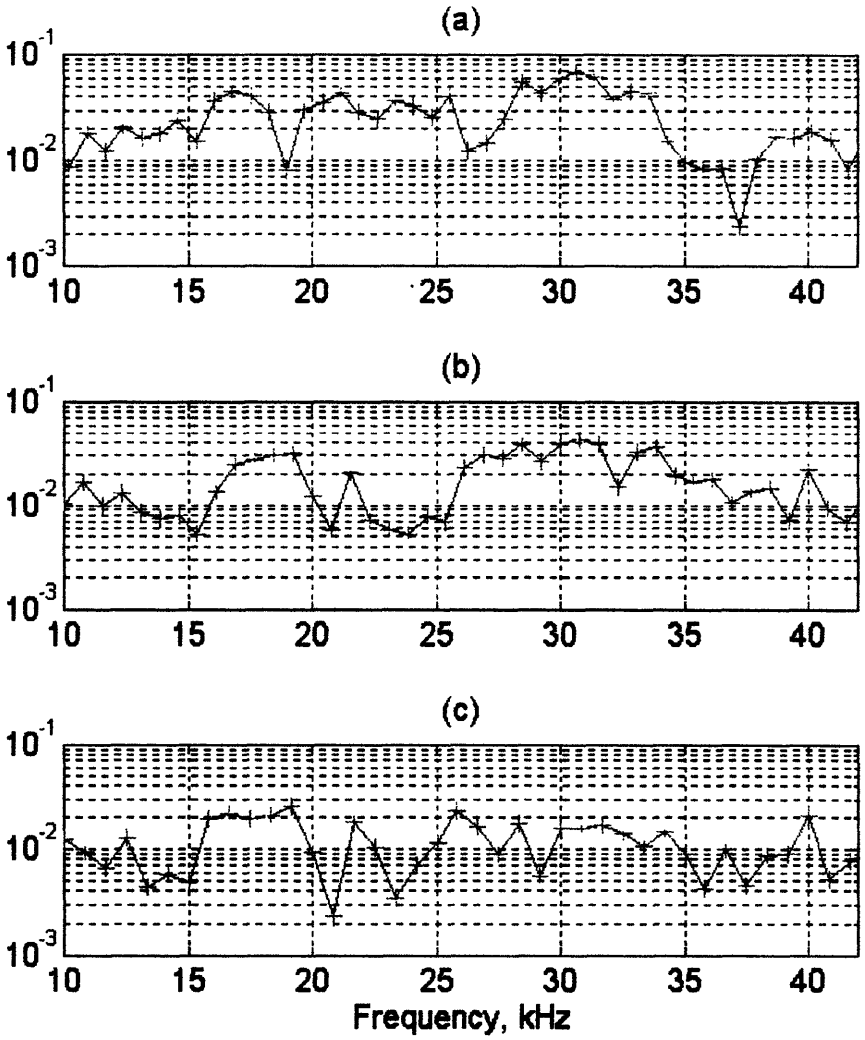

Fig 4.4.6 Magnitude of the Spectral Function of the Bandlimited Impulse Response of the Shell with Internal Structures at Beam Aspect for the period (a) 30 μsec < t < 1400 μsec, (b) 100 μsec < t < 1400 μsec, (c) 200 μsec < t < 1400 μsec

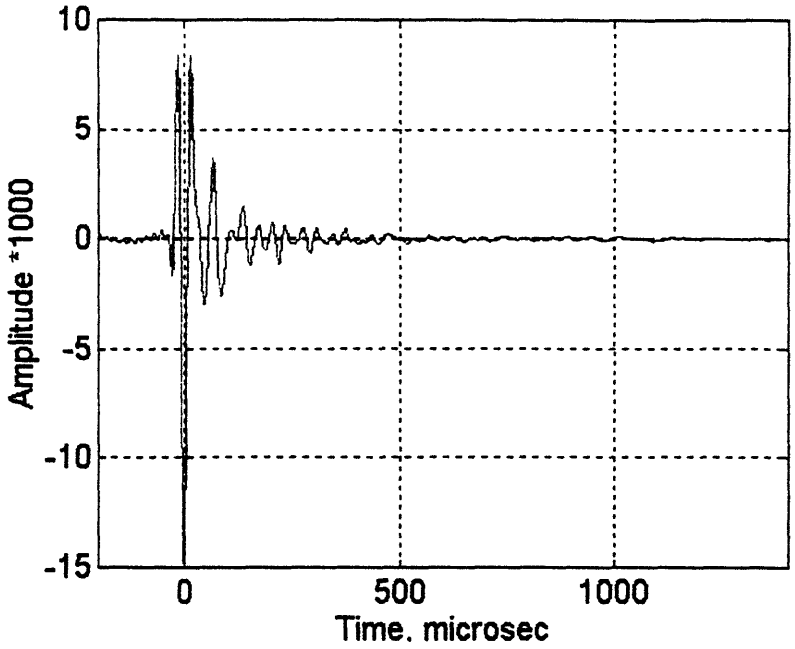

Fig 4.5.1 Measured Gaussian Bandlimited Impulse Response of the Layered Shell at Beam Aspect for a Frequency Range 2.75 < ka < 10.0 and a Radial Distance of r=2m from the Target Center.

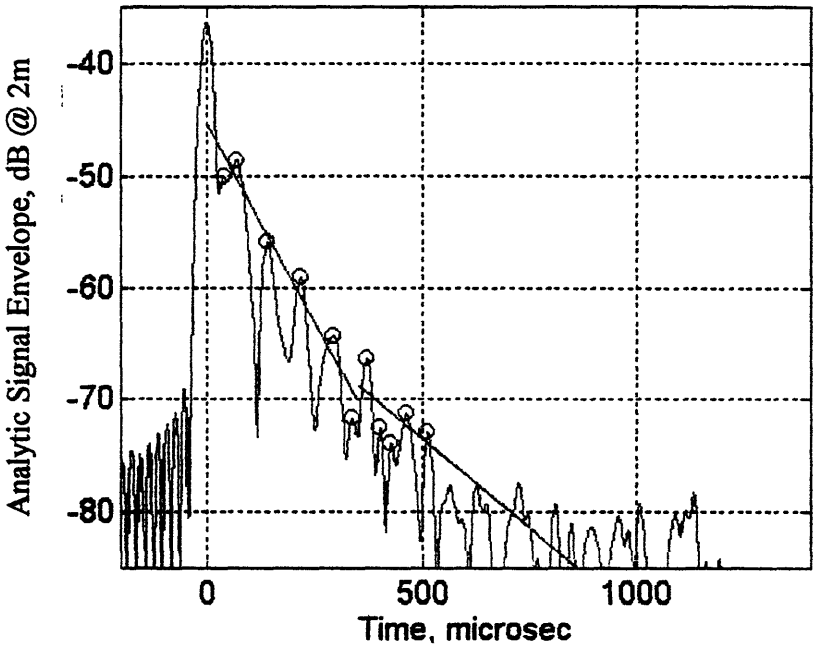

Fig 4.5.2 Logarithm of the Magnitude of the Envelope of the Gaussian Bandlimited Impulse Response of the Layered Shell at Beam Aspect. Levels less than -75dB are likely contaminated by noise.

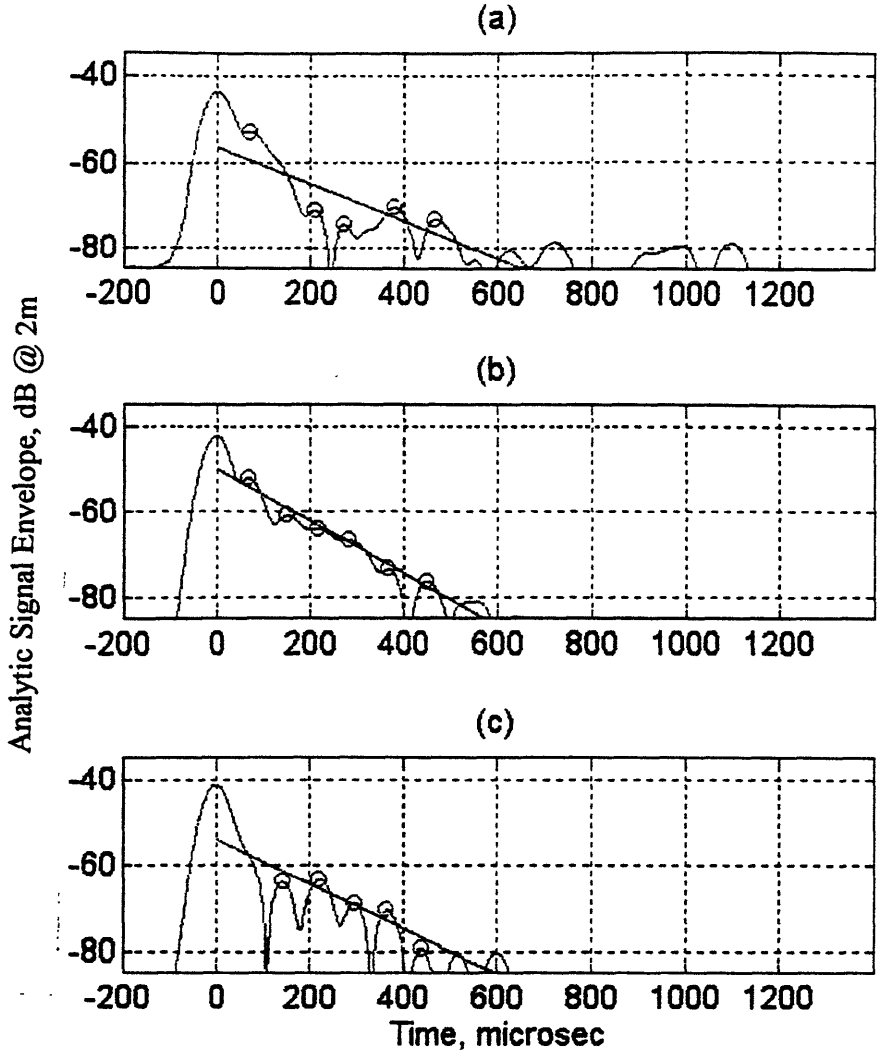

Fig 4.5.3 Logarithm of the Magnitude of the Envelope of the (a) Low Frequency Bandlimited Impulse Response (2.35 < ka < 5.64), (b) Mid Frequency Bandlimited Impulse Response (4.70 < ka < 7.99), (c) High Frequency Bandlimited Impulse Response (7.05 < ka <10.34), for Layered Shell at Beam Aspect.

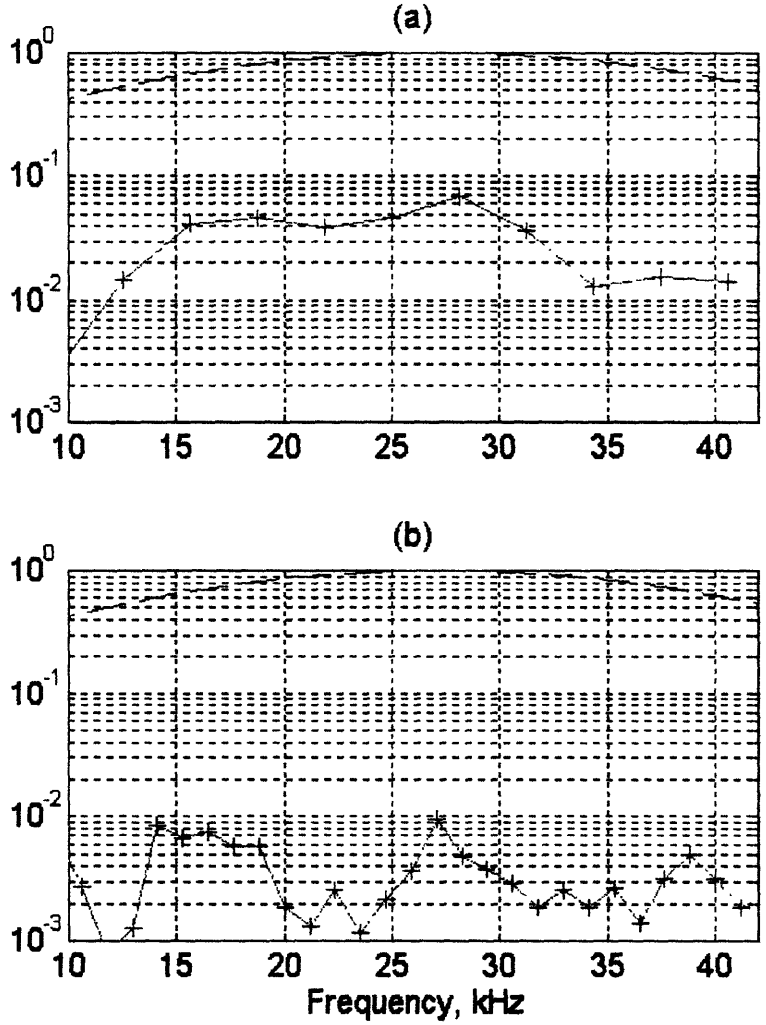

Fig 4.5.4 Magnitude of the Spectral Function of the Bandlimited Impulse Response of the Layered Shell for the period (a) 30 μsec < t < 350 μsec, (b) 350 μsec < t < 1200 μsec; break line shows the Gaussian Bandpass Filter

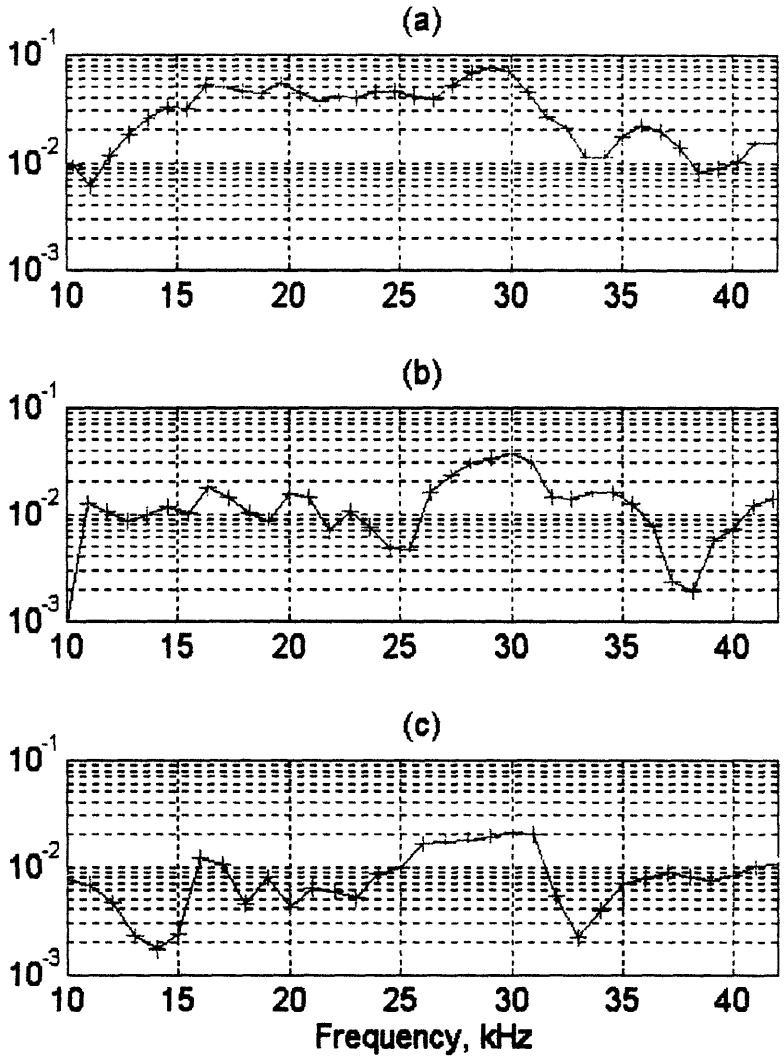

Fig 4.5.5 Magnitude of the Spectral Function of the Bandlimited Impulse Response of the Layered Shell at Beam Aspect for the period of (a) 30 μsec < t < 1200 μsec, (b) 100 μsec < t < 1200 μsec, (c) 200 μsec < t < 1200 μsec

5. Conclusion

The initial or geometric returns of the shells at beam aspect are -38.7dB re. r=2m for the empty shell, -38.5dB for the ring stiffened shell, -36.7dB for the internalled shell and -36.4dB for the layered shell, or about -37.6dB±1.1dB for all cases. These results are quite different from the simplified lumped-system model analysis, and shows that the distributed rings can not be modeled by a simple uniform extra mass on the shell. Because of the small range (±1.1dB), the role of internal structures and other complexities in the geometric return can be neglected.

The decay rates obtained from the beam aspect backscattering data are summarized in Table 5.1. First and subsequent decay rates are calculated for each bandwidth: total frequency band 12 - 42 kHz, low frequency band 10 - 24 kHz, mid frequency band 20 - 34 kHz, and high frequency band 30 - 44 kHz. The time that separates the first and subsequent decay rates are 350 μsec for the total frequency band, 450 μsec for the low frequency band, 350 μsec for the mid frequency band and 250 μsec for the high frequency band. These times are calculated from the round trip group delay through the shortest bay of the shell by the flexural wave in that frequency band. In the empty shell case, the round trip travel time by the flexural wave through the entire shell is around 1500 μsec, for which data are not available. Therefore, only the first decay rates are tabulated for the empty shell.

For the total frequency band, the first decay rate for the empty shell is higher than those for the shell with stiffening rings and the shell with internal structures only, and about the same as for the layered shell. The first decay rates for the empty shell do not change with frequency. The shell with stiffening rings and the shell with internal structures

have similar first decay rates. The added internal structures provide energy storage and the decay rates are less than the empty shell case, especially at low frequency where the decay rates for both are much smaller than the empty shell case. The decay rates are larger at high frequency. The layered shell is much like the empty shell, except that it has a little larger first decay rate because of damping on the shell. And the layered shell has different decay rates as a function of frequency.

Fig 5.1 compares the maxima from the envelope function for each shell. The empty shell and the layered shell have very similar decay patterns. Also, the shell with stiffening rings and the shell with internal structures have similar decay patterns. The influence of the rings and internal structures are best seen after 350 μsec; for the ringed shell and internalled shell, the decay is measureable to 1400 μsec, but for the layered shell it is quite weak due to the layer.

The induced compressional waves, which circumnavigate the shell, are the major source of the scattering process for the empty shell. From Fourier analysis, the empty shell radiates elastically mostly through the first and second ring frequencies. The measured major scattering frequencies are 16 kHz and 32 kHz. These are very close to the calculated first and second ring frequencies, 15kHz and 30kHz. The shell with the stiffening rings also has the same major elastic scattering frequencies as the empty shell. But the analysis in the later time period shows that these frequencies are shifted to higher frequencies by about 2kHz.

In all shells, the major source of the scattering is the induced compressional waves on the shell for the early time. But, for all but the empty shell, the stiffening rings store energy, and become a major source of scattering, and they radiate preferentially at the ring frequencies. In the shell with internal structures(internalled and layered), the attachments of the four rubber blocks influence radial ring motion to prefer the second ring frequency.

But late in time(after 200 μsec), the internal structures of the internalled shell only influence the scattering and there is no dominant scattering frequency. The internal structures of the layered shell however do not interact much with the shell even at the later time. Therefore, there is still preferential scattering through first and second ring frequencies. The damping along the shell reduces energy storage in the rings and internal structures, so they can not contibute as much to the radiation at a later time.

	Bandpass Filter			
	12kHz-42kHz	10kHz-24kHz	20kHz-34kHz	30kHz-44kHz
Empty Shell	0.064	0.065	0.065	0.063
Shell with Stiffened Rings	0.051	0.030	0.056	0.085
	0.011	0.0032	0.0066	0.0114
Shell with Internal Structures	0.045	0.032	0.078	0.076
	0.0081	0.0011	0.0108	0.0087
Layered Shell	0.071	0.044	0.061	0.052
	0.032			

Table 5.1 Decay Rates (dB/μsec) from the Logarithm of the Magnitude of the Envelope of the Gaussian Bandlimited Impulse Response. Where there are two entries, the top one is for the initial decay, the bottom for the subsequent decay. (Subsequent decay rates are obtained after 350 μsec for 12 - 42 kHz band, after 450 μsec for 10-24 kHz band, after 350 μsec for 20 - 34 kHz and after 250 μsec for 30 - 44 kHz.) Missing subsequent decay rates are caused by concern for noise contamination.

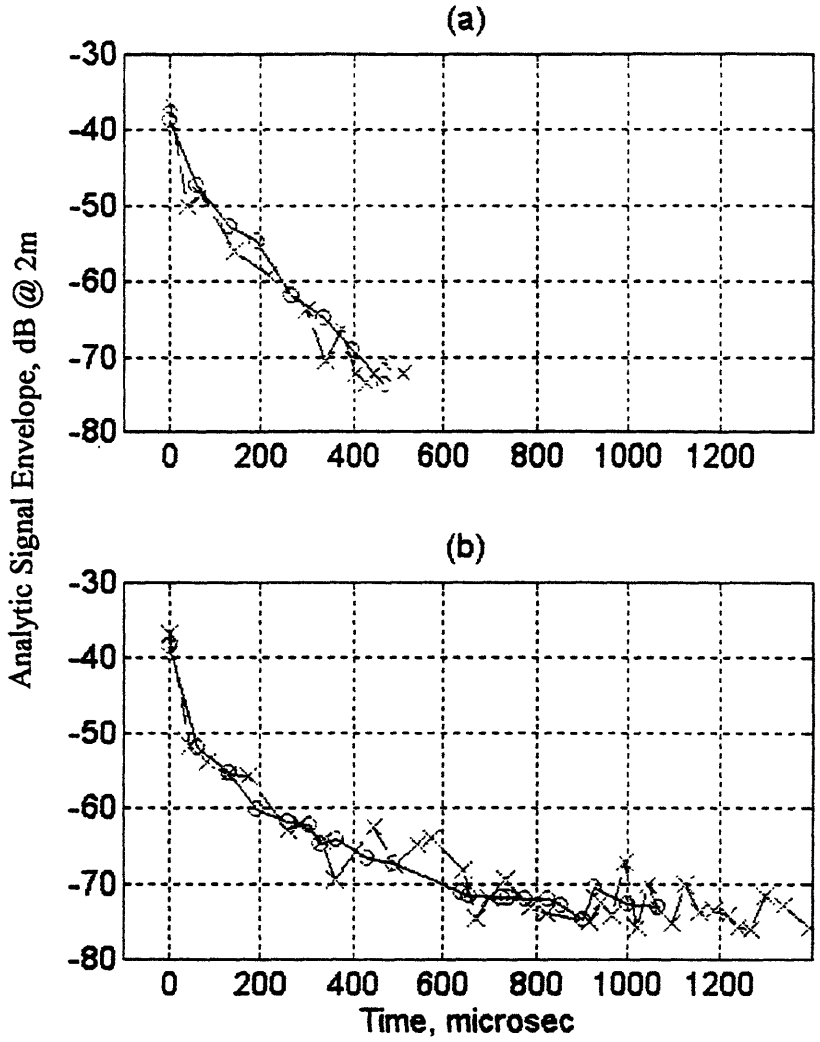

Fig 5.1 Maxima from the Logarithm of the Magnitude of the Envelope of the Gaussian Bandlimited Impulse Response, (a) o - Empty Shell, x - Layered Shell
(b) o - Shell with Stiffening Rings, x - Shell with Internal Structures.

Table of Figures

Table of Tables

References

[1] M. C. Junger, and D. Feit, *Sound, Structures, and Their Interaction*, (MIT Press, Cambridge, MA 1986)

[2] K. L. Williams and P. L. Marston, " Axial Focused (Glory) Scattering Due to Surface Waves Generated on Spheres: Model and Experimental Confirmation Using Tungsten Carbide Spheres", J. Acoust. Soc. Am., **78** (2), 772-728 (1985).

[3] S. G. Kargl and P. L. Marston, "Observation and Modeling of the Backscattering of Short Tone Bursts from a Spherical Shell: Laml Wave Echoes, Glory, and Axial Reverberations", J. Acoust. Soc. Am., **85** (3), 1014-1028 (1989).

[4] L. B. Felson, J. M. Ho, and I. T. Lu, "Three Dimensional Green's Function for Fluid-Loaded This Elastic Cylindrical Shell: Formulation and Solution", J. Acoust. Soc. Am., **87** (2), 543-553 (1990).

[5] L. B. Felson, J. M. Ho, and I. T. Lu, "Three Dimensional Green's Function for Fluid-Loaded This Elastic Cylindrical Shell: Alternative Representations and Ray Acoustic Forms", J. Acoust. Soc. Am., **87** (2) 554-569 (1990).

[6] L. B. Felson, J. M. Ho, and I. T. Lu, "Erratum: Three Dimensional Green's Function for Fluid-Loaded This Elastic Cylindrical Shell: Alternative Representations and Ray Acoustic Forms", J. Acoust. Soc. Am., **89** (3) 1463-1464 (1991).

[7] F. Leon, F. Lecroq, D. Decultot, and G. Maze, "Scattering of an Obliquely Incident Acoustic Wave by an Infinite Hollow Cylindrical Shell", **91** (3), 1388-1397 (1992).

[8] Y. P. Guo, "Sound Scattering from an Internally Loaded Cylindrical Shell", J. Acoust. Soc. Am., **91,** 926-938 (1992).

[9] Y. P. Guo, "Sound Scattering from Cylindrical Shells with Internal Elastic Plates", J. Acoust. Soc. Am., **93** (4), 1936-1946 (1993).

[10] C. N. Corrado Jr, "Mid-Frequency Acoustic Backscattering From Finite Cylindrical Shells and The Influence of Helical Membrane Waves", Ph.D Thesis, January 1993.

[11] I. Dyer and M. Conti, Memorandum dated 25 June, 1990, Subject: Scale Model Experiments on an Internally Loaded Cylinder.

[12] Personal Meeting with I. Dyer during January 1995.

[13] P. M. Morse nad K. U. Ingard, *Theoretical Acoustics*, (Princeton University Press, Princeton, New Jersey, 1968).

Appendix A

Lumped model analysis for infinite cylinders

Radiation from an infinitely long cylinder has been studied by Morse[13]. The equations which governs the radiation pressure field is the Helmholz Equation.

$$\nabla^2 p + k^2 p = 0 \qquad (1)$$

Equation (1) in cylindrical coordinate is

$$\frac{1}{r}\frac{\partial}{\partial r}\left(r\frac{\partial p}{\partial r}\right)+\frac{1}{r^2}\frac{\partial^2 p}{\partial \phi^2}+\frac{\partial^2 p}{\partial z^2}=0 \qquad (2)$$

We can solve Equation (2) by using the method of seperation of variables. First, we assume the solution of Equation (2) in the form

$$p = R(r)\Phi(\phi)Z(z)e^{-i\omega t} \qquad (3)$$

where R is a function of r alone, Φ is a function of ϕ alone and Z is a function of z alone. If (3) is introduced into equation (2), we get three ordinary differential equations

$$\frac{d^2 Z}{dz^2}+k_z^2 Z = 0 \qquad (4)$$

$$\frac{d^2 \Phi}{d\phi^2}+m^2\Phi = 0 \qquad (5)$$

$$\frac{1}{r}\frac{d}{dr}\left(r\frac{dR}{dr}\right)+(k_r^2-\frac{m^2}{r^2})R = 0 \qquad (6)$$

where m must be an integer for the solution to be continuous at ϕ=0=2π and, $k_z^2 + k_r^2 = k^2$.

Equation (4), (5) and (6) all have analytic solutions in the form of

$$Z \propto e^{ik_z z}, e^{-ik_z z}$$
$$\Phi \propto \cos m\phi, \sin m\phi$$
$$R \propto J_m(k_r r), N_m(k_r r)$$

We assume the cylinder as infinitely long so that there is no z dependence in the pressure field. Now we will only consider $\cos\phi$ as the angular dependence. Therefore, $k_z = 0$ and m=1. So, the pressure field solution is

$$p = A\cos\phi\left[J_1(kr)+iN_1(kr)\right]e^{i\omega t}$$

and when r=a

$$p = A\cos\phi\left[J_1(ka)+iN_1(ka)\right]e^{i\omega t}$$
$$= A\cos\phi H_1(ka)e^{i\omega t}$$

where, H(ka) is the Hankel function of first kind.

From the pressure field at r=a, we get the reaction force per unit length F in the x direction

$$F = \int_0^{2\pi} pa\cos\phi d\phi = Aa\pi H_1(ka)e^{-i\omega t}$$

From the relationship between the particle velocity and pressure

$$u_r = \frac{1}{i\omega\rho}\frac{\partial p}{\partial r}$$

$$= \frac{iA}{2\rho c}\cos\phi\left[H_2(ka) - H_0(ka)\right]e^{-i\omega t}$$

the velocity in the x direction is

$$U = \frac{iA}{2\rho c}\left[H_2(ka) - H_0(ka)\right]e^{-i\omega t}$$

and the impedence function is

$$\frac{F}{U} = i2\pi a\rho c\frac{H_1(ka)}{H_0(ka) - H_2(ka)}$$

The impedence function can be rewritten as

$$Z = -i\omega M_{rad} + R_{rad}$$

$$M_{rad} = \pi a^2\rho\frac{1}{ka}\mathrm{Im}(f(ka))$$

$$R_{rad} = \pi a\rho c\,\mathrm{Re}(f(ka))$$

$$f(ka) = 2i\frac{H_1(ka)}{H_0(ka) - H_2(ka)}$$

where M_{rad} is known as radiation mass or added mass and R_{rad} as radiation damping.

The impedence functions for the three different shell models which shown in Figure 3.2 are

$$Z_{empty} = -i\omega M + R_{rad}$$

$$M = M_{rad} + M_{shell}$$

$$Z_{ring} = -i\omega M + R_{rad}$$

$$M = M_{rad} + M_{shell} + M_{ring}$$

$$Z_{internal} = \frac{i}{\omega}\frac{\left[-\omega^2 M - i\omega(R_{rad} + R_s) + K_s\right]\left[-\omega^2 M_s - i\omega R_s + K_s\right] - \left[i\omega R_s - K_s\right]^2}{-\omega^2 M_s - i\omega R_s + K_s}$$

and each K_s and R_s are given by

$$\frac{K_s}{M_s} = \omega_0^2$$

$$R_s = \frac{0.1K_s}{\omega}$$

The impedence functions are derived previously from the radiation pressure field. From the ratio between radiation pressure field and incident pressure field, the impedence function can be expressed as,

$$Z_i = Z_r \frac{p_i(r=a)}{p_r(r=a)}$$

and, the ratio of the incident pressure field to radiation pressure field can be expressed as follows.

$$\frac{p_i}{p_r}(r=a) = 2i\frac{A_i}{A_r}\frac{J_1(ka)}{H_1(ka)}$$

$$\frac{A_r}{A_i} = \frac{-2i\left(1-\frac{\rho c}{\rho_0 c_0}\right)}{\left(1-\frac{\rho c}{\rho_0 c_0}\right)+i\left[\frac{N_1(ka)}{J_1(ka)}-\frac{\rho c}{\rho_0 c_0}\left(\frac{N_2(ka)-N_0(ka)}{J_2(ka)-J_0(ka)}\right)\right]}$$

ρc are the density and sound wave speed of the inside fluid and $\rho_0 c_0$ are those of the outside fluid.

From the impedence function Z, we can derive the frequency transfer function H.

$$H(ka) = \frac{F_{scatt}}{F_{ref}}(ka) = \frac{UR_{rad}}{F_{ref}}(ka) = \frac{R_{rad}}{Z}(ka)$$

Inverse Fourier Transform of the Gaussian filtered frequency transfer function leads to the Gaussian Impulse response function.

$$G(ka)H(ka) = \tilde{H}(ka)$$

$$\tilde{H}(ka) \underset{inv}{\rightarrow} \tilde{h}(t)$$

Appendix B

Natural modes of internal structures in the cylindrical shell

In this analysis, the delrin rod can have compressional and bending wave motions. But the stainless steel mass only has the role of mass which can have rotational and transitional inertia. For the coupling between the bending wave and longitudinal wave, the coupling constant *es* is given as an eccentricity which has the dimension of length. In this analysis 0.005m is taken for coupling constant. The variables and constants used in the equations are shown in Figure B.1.

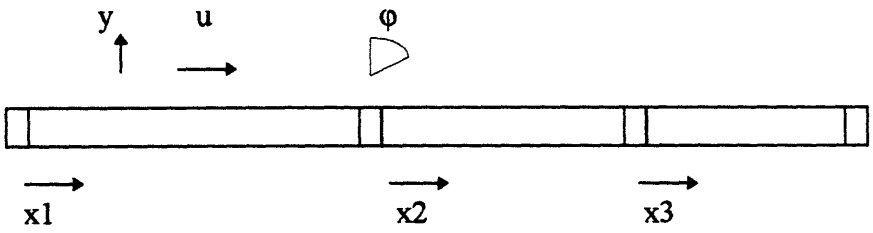

G: Shear modulus (1.4e9 N/m)
E: Young's modulus (3.7e9 N/m)
ρ_s: Density of the rod (1400 kg/m^3)
A: Cross-sectional area of the rod (5.067e-4 m^2)
I: Moment of inertia of the section (2.043e-8 m^4)
M: Mass of the stainless steel (0.068 kg)
Lm: Length of the stainless steel (0.0173 m)
J: Rotational inertia of the stainless steel (4.437e-6 kgm^2)
L1: Length of the first bay (0.2176 m)
L2: Length of the second bay (0.1727 m)
L3: Length of the third bay (0.1102 m)

Figure B.1 Variables and Constants used in analysis.

- Governing Equations

1 Timosenko Equation for bending motion [1]

$$G\kappa A\left(\frac{\partial^2 y}{\partial x^2}-\frac{\partial \varphi}{\partial x}\right)=\rho_s A\frac{\partial^2 y}{\partial t^2}$$

$$G\kappa A\left(\frac{\partial y}{\partial x}-\varphi\right)+EI\frac{\partial^2 \varphi}{\partial x^2}=\rho_s I\frac{\partial^2 \varphi}{\partial t^2}$$

or

$$EI\frac{\partial^2 y}{\partial x^4}+\rho_s I\frac{\partial^2 y}{\partial t^2}-\left(\rho_s I+\frac{EI\rho_s}{\kappa G}\right)\frac{\partial^4 y}{\partial x^2\partial t^2}+\rho_s I\frac{\rho_s}{\kappa G}\frac{\partial^4 y}{\partial t^4}=0$$

2 Equation for longitudinal motion [1]

$$\rho_s A\frac{\partial^2 u}{\partial t^2}=EA\frac{\partial^2 u}{\partial x^2}$$

- Boundary Conditions for coupled motion

@ x1=0

$$EA\frac{\partial u_1}{\partial x}=M\frac{\partial^2 u_1}{\partial t^2}$$

$$\kappa AG\left(\varphi_1-\frac{\partial y_1}{\partial x}\right)=-M\left(\frac{\partial^2 y_1}{\partial t^2}-\frac{Lm}{2}\frac{\partial^2 \varphi_1}{\partial t^2}\right)-k_l\left(y_1-\frac{Lm}{2}\varphi_1\right)$$

$$EI\frac{\partial \varphi_1}{\partial x}=J\frac{\partial^2 \varphi_1}{\partial t^2}+\frac{Lm}{2}\kappa AG\left(\varphi_1-\frac{\partial y_1}{\partial x}\right)-esEA\frac{\partial u_1}{\partial x}$$

@ x1=L1, x2=0

$$EA\frac{\partial u_1}{\partial x}=EA\frac{\partial u_2}{\partial x}-M\frac{\partial^2 u_2}{\partial t^2}$$

$$\kappa AG\left(\varphi_1-\varphi_2-\frac{\partial y_1}{\partial x}+\frac{\partial y_2}{\partial x}\right)=M\left(\frac{\partial^2 y_2}{\partial t^2}-\frac{Lm}{2}\frac{\partial^2 \varphi_2}{\partial t^2}\right)+k_l\left(y_2-\frac{Lm}{2}\varphi_2\right)$$

$$EI\left(\frac{\partial \varphi_1}{\partial x}-\frac{\partial \varphi_2}{\partial x}\right)=-J\frac{\partial^2 \varphi_2}{\partial t^2}-\frac{Lm}{2}\kappa AG\left(\varphi_2+\varphi_1-\frac{\partial y_2}{\partial x}-\frac{\partial y_1}{\partial x}\right)-esEA\left(\frac{\partial u_1}{\partial x}-\frac{\partial u_2}{\partial x}\right)$$

$$u_1=u_2$$

$$\varphi_1=\varphi_2$$

$$y_1=-Lm\varphi_2+y_2$$

@ x2=L2, x3=0

$$EA\frac{\partial u_2}{\partial x} = EA\frac{\partial u_3}{\partial x} - M\frac{\partial^2 u_3}{\partial t^2}$$

$$\kappa AG\left(\varphi_2 - \varphi_3 - \frac{\partial y_2}{\partial x} + \frac{\partial y_3}{\partial x}\right) = M\left(\frac{\partial^2 y_3}{\partial t^2} - \frac{Lm}{2}\frac{\partial^2 \varphi_3}{\partial t^2}\right) + k_l\left(y_3 - \frac{Lm}{2}\varphi_3\right)$$

$$EI\left(\frac{\partial \varphi_2}{\partial x} - \frac{\partial \varphi_3}{\partial x}\right) = -J\frac{\partial^2 \varphi_3}{\partial t^2} - \frac{Lm}{2}\kappa AG\left(\varphi_3 + \varphi_2 - \frac{\partial y_3}{\partial x} - \frac{\partial y_2}{\partial x}\right) - esEA\left(\frac{\partial u_2}{\partial x} - \frac{\partial u_3}{\partial x}\right)$$

$$u_2 = u_3$$

$$\varphi_2 = \varphi_3$$

$$y_2 = -Lm\varphi_3 + y_3$$

@ x3=L3

$$EA\frac{\partial u_3}{\partial x} = -M\frac{\partial^2 u_3}{\partial t^2}$$

$$\kappa AG\left(\varphi_{31} - \frac{\partial y_3}{\partial x}\right) = M\left(\frac{\partial^2 y_3}{\partial t^2} + \frac{Lm}{2}\frac{\partial^2 \varphi_3}{\partial t^2}\right) + k_l\left(y_3 + \frac{Lm}{2}\varphi_3\right)$$

$$EI\frac{\partial \varphi_3}{\partial x} = -J\frac{\partial^2 \varphi_3}{\partial t^2} - \frac{Lm}{2}\kappa AG\left(\varphi_3 - \frac{\partial y_3}{\partial x}\right) - esEA\frac{\partial u_3}{\partial x}$$

- Dispersion relations of the bending wave number β and frequency ω

$$EI\,\beta^4 + \left(\rho_s I + \frac{EI\rho_s}{G\kappa}\right)\omega^2\beta^2 + \rho_s I\frac{\rho_s}{G\kappa}\omega^4 - \rho_s A\omega^2 = 0$$

$$\beta^2{}_1 = \frac{1}{2a}\left(-b + \sqrt{b^2 - 4ac}\right)$$

$$\beta^2{}_2 = \frac{1}{2a}\left(-b - \sqrt{b^2 - 4ac}\right)$$